FABRICATION AND CHARACTERIZATION OF SERS SUBSTRATES VIA LASER INDUCED PHOTOCHEMICAL SURFACE ROUGHENING OF SILICON

A THESIS SUBMITTED TO
THE GRADUATE SCHOOL OF NATURAL AND APPLIED SCIENCES
OF
MIDDLE EAST TECHNICAL UNIVERSITY

BY

ALP AKBIYIK

IN PARTIAL FULFILLMENT OF THE REQUIREMENTS
FOR
THE DEGREE OF MASTER OF SCIENCE
IN
PHYSICS

JUNE 2022

Approval of the thesis:

FABRICATION AND CHARACTERIZATION OF SERS SUBSTRATES VIA LASER INDUCED PHOTOCHEMICAL SURFACE ROUGHENING OF SILICON

submitted by **ALP AKBIYIK** in partial fulfillment of the requirements for the degree of **Master of Science in Physics Department, Middle East Technical University** by,

Prof. Dr. Halil Kalıpçılar
Dean, Graduate School of **Natural and Applied Sciences** _____

Prof. Dr. Seçkin Kürkcüoğlu
Head of Department, **Physics** _____

Assoc. Prof. Dr. Alpan Bek
Supervisor, **Physics, METU** _____

Examining Committee Members:

Assoc. Prof. Dr. Burak Ülgüt
Chemistry Department, Bilkent University _____

Assoc. Prof. Dr. Alpan Bek
Physics Department, METU _____

Assoc. Prof. Dr. Emre Yüce
Physics Department, METU _____

Date: 10.06.2022

I hereby declare that all information in this document has been obtained and presented in accordance with academic rules and ethical conduct. I also declare that, as required by these rules and conduct, I have fully cited and referenced all material and results that are not original to this work.

Name, Surname: Alp Akbıyık

Signature :

ABSTRACT

FABRICATION AND CHARACTERIZATION OF SERS SUBSTRATES VIA LASER INDUCED PHOTOCHEMICAL SURFACE ROUGHENING OF SILICON

Akbıyık, Alp
M.S., Department of Physics
Supervisor: Assoc. Prof. Dr. Alpan Bek

June 2022, 61 pages

In this thesis, Surface-Enhanced Raman Spectroscopy (SERS) substrates are fabricated using laser assisted chemical etching of silicon as a surface nanostructuring technique. As a novel method of control over the structuring parameters, the incident laser illumination is spatially modified via a Digital Micromirror Device (DMD) that enable fast and uniform fabrication of complex structures. Onto the photochemically nanostructured silicon surfaces, silver and gold films are deposited by thermal evaporation or nanoparticles are formed to transform the roughened Si surfaces into the SERS substrates. The thickness of Ag and Au on the structured Si is shown to significantly alter the SERS spectra. The increase of the SERS signal is also attributed to the electromagnetic field enhancement that result from the surface roughness of Si which is controlled by the illumination power, duration and the spot size of the laser beam. For the characterization of the SERS substrates, Raman spectra of the dye molecule Brilliant Cresyl Blue (BCB) can be observed down to nM orders. Fabricated substrates are also compared under 660 nm and 532 nm excitations. Nanostructured Si surface with Ag deposition is shown to create more enhancement than Au deposition

under 532 nm excitation with an enhancement factor (EF) up to 10^9. EF is calculated and SERS performance is evaluated based on both SERS and dark-field scattering spectra experimentally, and using Finite-Difference Time-Domain (FDTD) simulations, numerically. Further range of applicability of the substrates are investigated by testing with the molecules Crystal Violet (CV), Rhodamine 6G and ammonium nitrate from which large enhancements are obtained.

Keywords: Laser-assisted chemical etching, surface roughening of silicon, Surface-Enhanced Raman Spectroscopy, SERS substrate

ÖZ

YÜZEY ARTIRIMLI RAMAN SAÇILMASI ALTTAŞLARININ LAZERLİ FOTOKİMYASAL YÜZEY İŞLEMEYLE ÜRETİMİ VE KARAKTERİZASYONU

Akbıyık, Alp
Yüksek Lisans, Fizik Bölümü
Tez Yöneticisi: Doç. Dr. Alpan Bek

Haziran 2022 , 61 sayfa

Bu tez çalışmasında, lazer yardımlı fotokimyasal yüzey aşındırma yöntemiyle yapılandırılan kristal silikon yüzeyinden Yüzey Artırımlı Raman Spektroskopisi alttaşları üretilmiştir. Fotokimyasal aşındırmada kompleks yapılarda hızlı ve kesin kontrol sağlayan ve yenilikçi bir yöntem olarak lazer ışığı uzamsal olarak DMD (Dijital Mikroayna Cihazı) ile modüle edilmiştir. Aşındırılmış silikon yüzeyin üstüne plazmonik sıcak noktalar oluşturmak amacıyla termal buharlaştırma yöntemiyle altın ve gümüş filmler kaplanmış, ayrıca altın ve gümüş nanoparçacıklar oluşturulmuştur. Aşındırılmış yüzeyin üstündeki altın ve gümüş film veya parçacık kalınlığının elde edilen Raman sinyalini önemli ölçüde değiştirdiği görülmüştür. Bununla birlikte aşındırılmış yüzeydeki pürüzlülük parametrelerinin de elektromanyetik artırımı önemli ölçüde değiştirdiği ve artırdığı gösterilmiştir. Bu aşındırma parametreleri arasında Raman sinyaline önemli etki edenler lazer ışıma gücü, aydınlatma süresi ve aydınlatılan alanın boyutudur. Elde edilen alttaşların Raman artırımı karakterizasyonu üzerine BCB, CV, R6G ve amonyum nitrat molekülleri damlatılarak yapılmıştır. Raman spektroskopi-

sinde ışıma dalgaboyları olarak 532 nm ve 660 nm kullanılmıştır. BCB'den gelen Raman sinyali nanomolar seviyelere kadar gözlenmiştir. Yapılan deneysel, teorik ve bilgisayarlı hesaplamalara göre artırım faktörü 50 nm gümüş kaplı aşındırılmış silikon yüzey için 10^9 mertebelerine varmaktadır.

Anahtar Kelimeler: lazer yardımlı kimyasal işleme, silikon yüzey pürüzlendirmesi, Yüzey artırımlı Raman saçılması, Yüzey artırımlı Raman saçılması alttaşı

to my family

ACKNOWLEDGMENTS

First, I want to thank my supervisor Alpan Bek for encouraging me throughout my study and help me conduct research independently. And I want to thank Emre Yüce for supporting my study in his laboratory and contributing with his ideas.

I express my gratitude to my friends and colleagues in nano-optics and GÜNAM groups who make my time in METU enjoyable.

My special thanks are for Sena who becomes my greatest supporter during the course of my thesis, and for my parents for supporting me in every step of my education.

I hereby acknowledge the financial support from The Scientific and Technological Research Council of Turkey (TÜBİTAK) under grant numbers 119F101 and 2210E throughout my master's education.

TABLE OF CONTENTS

LIST OF TABLES

TABLES

LIST OF FIGURES

FIGURES

LIST OF ABBREVIATIONS

SERS	Surface-Enhanced Raman Spectroscopy
LSPR	Localized Surface Plasmon Resonance
EM	Electromagnetic
CE	Chemical Enhancement
EF	Enhancement Factor
LACE	Laser-Assisted Chemical Etching
PEC	Photoelectrochemical
DMD	Digital Micromirror Device
LOD	Limit of Detection
n-Si	n-type Silicon
p-Si	p-type Silicon
AgNP	Silver Nanoparticles
AuNP	Gold Nanoparticles
AFM	Atomic Force Microscopy
SEM	Scanning Electron Microscope
PVD	Physical Vapour Deposition
BCB	Brilliant Cresyl Blue
CV	Crystal Violet
M	Molar
CCD	Charge-coupled Device
CW	Continuous Wave
FDTD	Finite-Difference Time-Domain

CHAPTER 1

INTRODUCTION

The research conducted in this thesis work demonstrate the cost and time effective large-area fabrication of SERS substrates by laser-induced photochemical etching of crystalline Si as a template for hot-spots. Upon the deposition of materials that exhibit plasmon response in the excited wavelengths, large values of enhancements with EF about 10^8 are obtained from the Raman spectra of the analyte molecules adsorbed on the fabricated substrates. A major advantage is that despite the random formations of nano-holes throughout the Si surface, the overall structure distribution can be controlled via laser parameters and the order of the enhancement largely depends on the deposited material thickness which can also be monitored.

Understanding and applying the principles of physics in micro and nano scales do not only serve us for that particular scale, also they can create a big impact for macro and meso-scale applications. Examples consist of various interdisciplinary fields and incidents ; from energy harvesting to diagnose of diseases, from detecting environmental pollution to preventing spread of a virus can rely on the methods of sensing, detecting and imaging in the scale of micro and nanometers exploiting the phenomena at the very heart of optics and electronics.

Raman spectroscopy is such kind of technique that covers plenty of application areas not only in physics but also in nanoscience, material science, chemistry, biology, and industry. And this technique is and essentially based on a very fundamental phenomenon, that is, a type of inelastic scattering of light inside the material. In this way, one can observe the vibrational signature of a sample to be examined. And vibrational spectrum is unique to those materials and their bonding scheme, depending on the change in polarization under excitation [8].

The problem that bothered the scientific community in the last decades is that Raman spectroscopy itself of material usually has a low signal-to-noise ratio, especially when examining the trace amounts of an analyte molecule. Without having sufficient signal quality, the spectroscopy technique would have no use in investigating the materials which may be found as composite structures, in small amounts, or diluted. In this challenging obstacle, plasmonic nanostructures paved the way for analyzing any kind of Raman-active molecule by enhancing the electromagnetic field exponentially in the proximity of the analyte molecule which gave rise to the concept of "surface-enhanced Raman spectroscopy"[9]. In the last few decades, SERS substrates are fabricated by numerous techniques from adsorbing noble metal nanoparticles [10] to applications of various surface structuring techniques onto a substrate material.

Nanostructuring of the surfaces in the subwavelength regime provides uniform and effective enhancing possibilities to the substrate and takes the advantage of fabricating desired nanostructure shape instead of chemically synthesizing nanoparticles using various chemicals that can interfere SERS signal and reduce reproducibility due to their complex reaction dynamics. Moreover, since the plasmon resonance is directly altered by shape modification of metal nanostructure, morphology-dependent modes with an improved scattering response can arise from nanostructured substrates. The top-down nano-processing methods vary from reactive ion etching (RIE), electron-beam [11] to laser-induced periodic surface structures (LIPSS) [12] and wet etching techniques [13, 14, 15, 16] driven by electrodes, metal or illumination. All these techniques have both advantages and disadvantages in terms of precision, reproduction, cost-effectiveness, and time [17]. Dry patterning techniques such as ion beam or e-beam can be notably precise and widely useful however they have more time and fabrication costs compared to wet etching techniques. This thesis work demonstrates the effective fabrication of large-area, low-cost photochemically nanostructured Si-based SERS substrates, of which design can be adjusted for various excitation wavelengths and analyte molecules by controlling nanostructuring parameters, deposited metal film and nanoparticles, and deposition thickness.

CHAPTER 2

LITERATURE SURVEY

2.1 Surface-Enhanced Raman Spectroscopy

Before demonstrating the research of the fabricated Surface-Enhanced Raman Spectroscopy (SERS) substrates for thesis studies and substrate fabrication methods in detail, it is more plausible to briefly introduce Raman scattering itself, and the Localized Surface Plasmon Resonance phenomena which constitute the SERS technique we use today [18, 19, 20]. Combining two aforementioned phenomena, SERS substrates reveal the trace amounts of molecules and contribute to the current literature on the detection of explosives, pollutants, harmful chemicals, and biological substances by relying on nano-fabrication methods and mainly electromagnetic enhancement mechanism due to generation of hot-spots [21]. Although chemical enhancement due to charge transfers between molecule and substrate is an alternative source of enhancement, it is not systematically studied or observed within the scope of this work.

2.1.1 Raman Scattering and Spectroscopy

Examining the light-matter interaction in the form of spectroscopy comes with a few types of configuration; absorption, luminescence (emission, in general), and scattering. Absorption is a one-step process that occurs via the transition of an electron from one state to a higher excited state with energy transfer of the photon, e.g dye molecule under illumination. Electronic absorption is used in spectroscopy when examining nanostructures of which lengths are compared with the UV-Visible range, which is also named the spectroscopy technique. Fluorescence, on the other hand, requires two steps, the transition of an electron via electronic absorption to the higher

state, then, relaxing into a vibrational state, emitting a lower energy photon [22, 23]. This difference in the wavelengths of absorption and luminescence peaks is called "Stokes shift". Emission types and related spectroscopy are more diverse and complicated than mentioned here and cover the whole EM spectrum, however, we shall now deal with the scattering of light. Light is scattered in two ways; as elastic and inelastic scattering. When an object is illuminated, the scattered light we most intensely observed is the Rayleigh (elastic) scattering, where incident and scattered photon have the same energy. In contrast, Raman scattering is an inelastic scattering, where there is energy transfer as the photon scatters from the molecule.

Raman scattering was first scientifically observed and characterized by C.V. Raman a century ago [24]. The observed Raman lines are attributed as "a new radiation" or "weak fluorescence" in the very first proposals back then, since the scattered intensity is several orders of magnitude less than fluorescence [24, 22]. Although this analogy is sensible, an important distinction of Raman scattering from fluorescence is that, there occurs no electronic absorption and re-emitting of the photon. Quantum mechanically, the incident photon is excited to an intermediate state between electronic states, then, emitted down to a vibrational state. An overall comparison of fluorescence and scattering types is shown in Figure 2.1 on the Jablonski diagram and modeled in Figure 2.2. Another main difference is that fluorescent particles have longer life-time in the order of nanoseconds, whereas in the scattering, it is less than femtoseconds [23].

In order to be examined by Raman spectroscopy, an analyte molecule or crystal should be Raman active. Raman active means that change in polarizability occurs while molecules are vibrating due to excitation, whereas, polarizability is the tendency of electrons of the molecule to be perturbed by an external electric field [8]. Charge configurations in a molecule can be understood by induced dipole moment equation :

$$\mathbf{p} = \alpha \mathbf{E}. \tag{21}$$

Although polarizability (α) will be revisited in the localized surface plasmon section as a response of metal structures to the external electric field, we are now only

concerned with the change in polarization of the molecules with various bonds. Usually, symmetrical vibrations that extend the bonds are Raman-active since there is a change in polarizability. However, if the vibrations cause the change in dipole moment instead, the molecule is Raman-inactive but IR-active. This occurs usually with bending and asymmetric stretching vibrations where the bond length does not change, but the dipole moment changes [8]. Raman active and inactive bands can be complementary in a molecule that contains different vibration configurations. Numerous organic molecules and crystals are generally Raman-active due to their Raman favorable molecular degrees of freedom.

In Raman spectroscopy technique, a sample to be examined is illuminated by a coherent light source. Rayleigh scattered part is filtered in order to be left with the Raman scattered light. That part passes through a diffraction grating in order to decompose of its components. The resulting signal is projected onto a CCD camera and can be analyzed through a software. Depending on the substrate and analyte molecule, fluorescent peaks may suppress Raman signal. A suitable excitation source from UV to NIR can be chosen in order to obtain sharply resolved high intensity Raman peaks by taking into account the degradation of the sample due to excitation.

Apart from SERS applications which will further be investigated in the rest of the thesis, Raman spectroscopy itself is eminently a useful characterization technique for various amorphous or crystal structures, 2D or bulk materials, etc. [25, 8]. This is because vibrational modes and scattered intensity would change, i.e shifts in the wavevector space and intensity would be observed, whether a material is amorphous or crystal, also depending on having defects, being porous or flat. Monolayer, bilayer and multilayered materials with the same atoms also have different linewidths and peak intensities. For instance, graphene and its derivatives can be fabricated in many forms such as monolayer sheet, multilayers, or flakes. Under the Raman spectroscopy, each formation would have different Raman peaks, though centered in the same k-vector, linewidth and intensity profile would change. Then, we could determine its material characteristics from the spectroscopy.

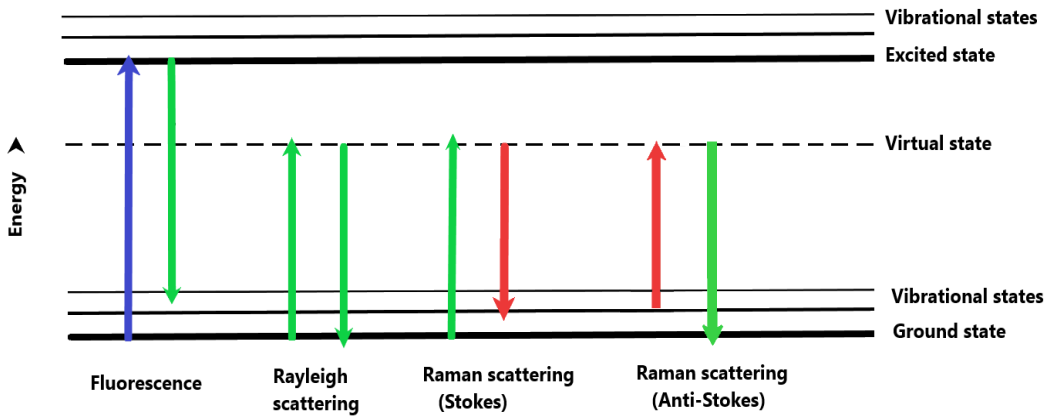

Figure 2.1: Jablonski diagram of the energy states for various optical interactions.

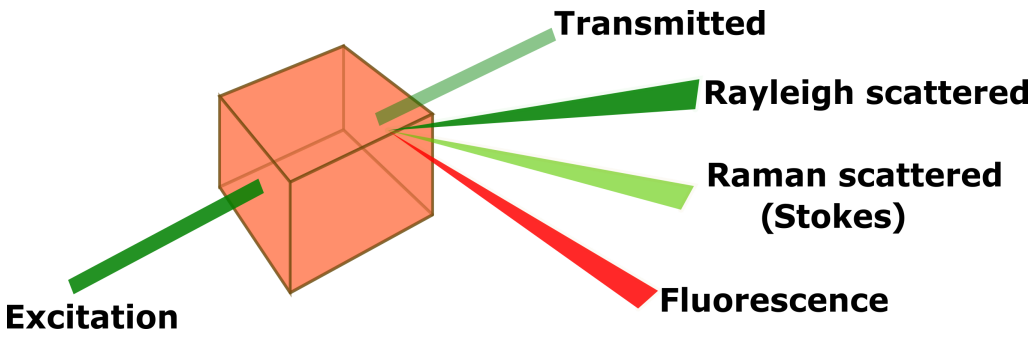

Figure 2.2: A comparative model representation of Jablonski diagram above on a substrate under excitation.

2.1.2 Enhancing Raman Signals : Plasmonic Nanostructures

The field of plasmonics covers a wide range of literature of photon-electron interaction and resulting applications from waveguides to sensing, nano-antennas to near-field spectroscopy. Here, we approach plasmonics from an elementary point of view to elaborate more on the enhancement mechanism behind the SERS substrates. The propagation or confinement vary with the system geometry and material, for instance, in the bulk plasmon case, resultant waves are longitudinal, in the surface plasmon case, coupling of light is achieved via specific conditions [26, 17] to propagate in

transverse waves, and the Localized Surface Plasmon case, oscillations occur due to restoring force from the closed geometry of the nanoparticle. The general overview of plasmonic models in different systems and resultant plasmon responses are given as example graphs in the Figures 2.3,2.4,2.5,2.6,2.7. A common principle of all the plasmon configurations is that plasmons are the collective oscillations of electrons, whether on the bulk metal, thin-film interface between metal and dielectric or confined into the structures such as nano-spheres, bowties, nano-cubes, etc. To start with the basics and examples, we shall first consider the origin of the plasmon resonance from the motion of electric charges, which then, brings us to our focus for SERS enhancement, localized surface plasmons. [27, 28, 29].

The most basic plasmon model is derived from the equation of motion of the electrons in a bulk metal as follows :

$$m\ddot{x} = -e\mathbf{E}, \tag{22}$$

where electric field has the plane-wave solution as,

$$\mathbf{E(t)} = E_0 e^{-i\omega t}. \tag{23}$$

While electrons change position with respect to nucleus, it induces a polarization field as $P = -Nex$. The resultant plasmon frequency is denoted as

$$\omega_p = \sqrt{\frac{Ne^2}{\epsilon_0 m}}. \tag{24}$$

For large enough frequencies where damping due to collisions can be neglected, dielectric function becomes as follows :

$$\epsilon_\omega = 1 - \frac{\omega_p^2}{\omega^2}. \tag{25}$$

In a more realistic case where loss of energy occurs due to internal interactions with

phonons, dielectric function in Drude model turns into [17] :

$$\epsilon_{metal} = 1 - \frac{\omega_p^2}{\omega^2 + i\omega\Gamma}. \tag{26}$$

Solving the wave equation of the electric field, the dispersion relation for the bulk plasmons becomes as plotted in Figure 2.4. Geometry changes the resonance frequency, for instance, the sphere has a resonance frequency of $\frac{\omega_p}{\sqrt{3}}$ while 2D film has $\frac{\omega_p}{\sqrt{2}}$.

$$\omega(k) = \sqrt{\omega_p^2 + c^2k^2}. \tag{27}$$

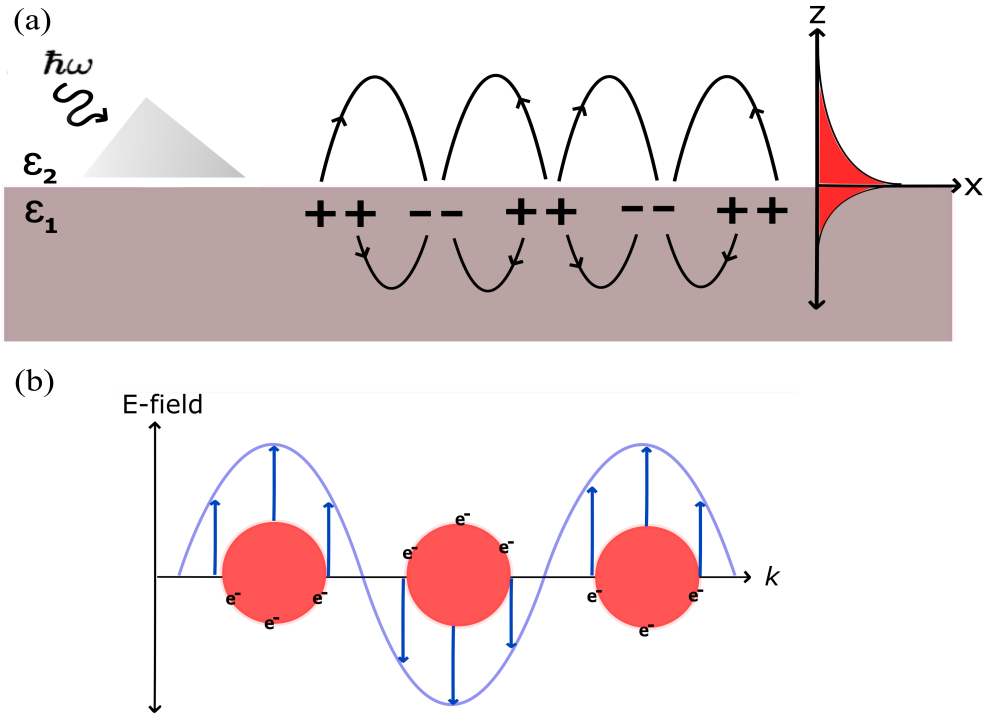

Figure 2.3: a) Schematic representation of propagating Surface Plasmon Polariton on the metal-dielectric interface. b) Localized Surface Plasmon Resonance model represented via spherical nanoparticle excited from the x-axis.

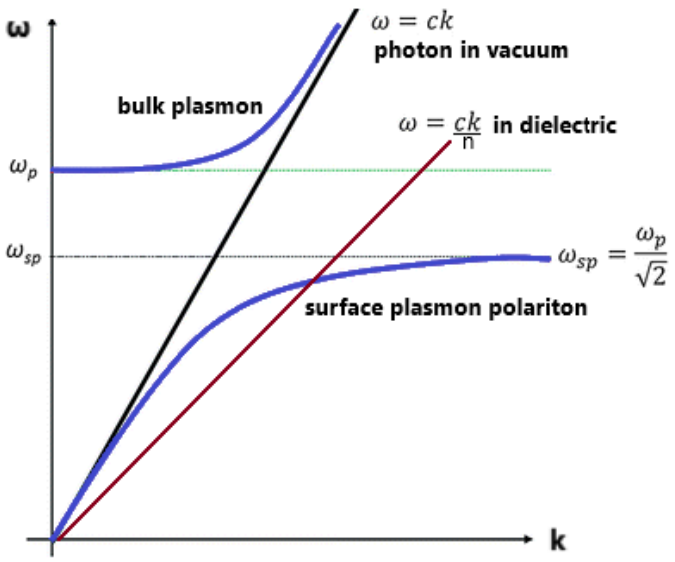

Figure 2.4: Surface-Plasmon Polariton dispersion curve compared with photon dispersion in air.Adopted from the reference [5] Bulk plasmon denotes the longitudinal wave oscillations of charges along the bulk metal, therefore cannot be excited by light, which is a transverse wave.

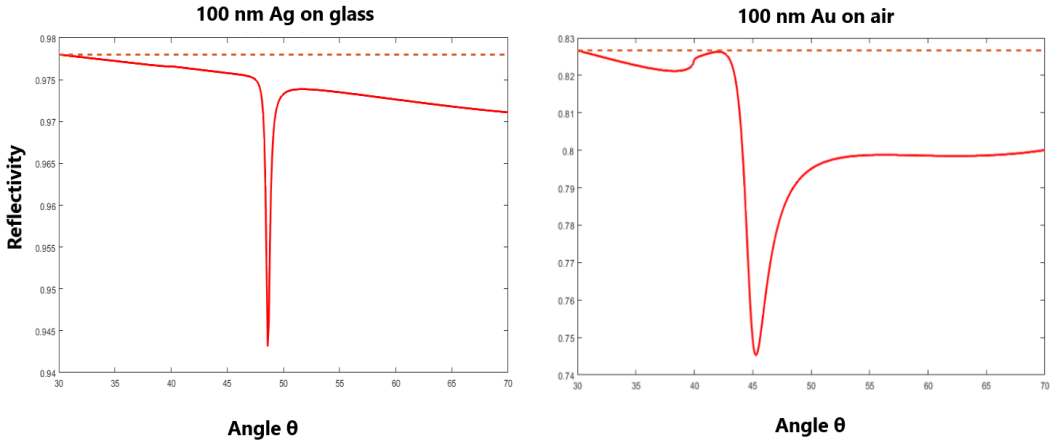

Figure 2.5: Reflectivity versus incident angle of 532 nm excitation coming from glass prism onto 100 nm silver and gold films with dielectric interfaces.

2.1.2.1 Plasmon Resonance and Localized Surface Plasmons

Localized Surface Plasmon Resonance (LSPR) are in the same manner, coherent oscillations of electrons. However, as the name suggests, localized plasmons do not propagate but they are confined in a nanostructure. Then, instead of equation of motion solutions, LSPR model can simply be treated as Laplace's equation for electric potential inside and outside the particular geometry. LSPR may emerge in numerous forms of metallic structures; from wires to blocks of spheres, gaps between two structures, triangles etc. as shown in Figure 2.6. Working on different geometries requires another thesis work and and loads of different equations, yet, we can derive a plasmon response from a basic symmetrical case, a noble metal sphere smaller than excited wavelength. By considering smaller sizes we can work on dipole resonance case in a quasi-static approach assuming uniform electric field [26, 30, 17, 27, 29].

Let us work out the small metal sphere model under uniform electric field by solving Laplace's equation for electric potential in spherical coordinates with the general form $\nabla^2\Phi = 0$:

$$\frac{1}{r^2 sin\theta}\left[sin\theta\frac{\partial}{\partial r}(r^2\frac{\partial}{\partial r}) + \frac{\partial}{\partial\theta}(sin\theta\frac{\partial}{\partial\theta}) + \frac{1}{sin\theta}\frac{\partial^2}{\partial\phi^2}\right]\Phi(r,\theta,\phi) = 0. \tag{28}$$

The general solution for this equation motivated by separation of variables and Legendre polynomials is written as below considering the azimuthal symmetry :

$$\Phi(r,\theta) = \sum_{l=0}^{\infty}\left(A_l r^l + B_l r^l + \frac{C_l}{r^{l+1}}\right)P_l(cos\theta) \tag{29}$$

The first term with A_l coefficient denotes the potential inside, whereas the rest of the terms denote the potential outside, which is the sum of scattered and incoming fields. Applying boundary conditions on the surface where $r = a$ for the sphere with dielectric constant ϵ and the surrounding medium is the vacuum with ϵ_0;

$$\left[\frac{\partial\Phi_{in}}{\partial\theta}\right]_{r=a} = \left[\frac{\partial\Phi_{out}}{\partial\theta}\right]_{r=a}, \tag{210}$$

$$\left[\epsilon\frac{\partial\Phi_{in}}{\partial r}\right]_{r=a} = \left[\epsilon_0\frac{\partial\Phi_{out}}{\partial r}\right]_{r=a} \tag{211}$$

We obtain the following solutions of potentials in and out of the sphere :

$$\Phi_{in} = -E_0 r cos\theta\Big(\frac{3\epsilon_0}{\epsilon+2\epsilon_0}\Big) \tag{212}$$

$$\Phi_{out} = -E_0 cos\theta\Big(r - \frac{a^3}{r^2}\frac{\epsilon-\epsilon_0}{\epsilon+2\epsilon_0}\Big) \tag{213}$$

leading to the electric field solutions using gradient of the potential as $\mathbf{E} = -\nabla\Phi$:

$$\mathbf{E}_{in} = \mathbf{E}_0\frac{3\epsilon_0}{\epsilon+2\epsilon_0} \tag{214}$$

$$\mathbf{E}_{out} = \mathbf{E}_0 + \frac{1}{4\pi\epsilon_0}\frac{3\mathbf{n}(\mathbf{n}\cdot\mathbf{p})-\mathbf{p}}{r^3} \tag{215}$$

where;

$$\mathbf{p} = 4\pi\epsilon_0 a^3\mathbf{E}_0\frac{\epsilon-\epsilon_0}{\epsilon+2\epsilon_0} \tag{216}$$

Using the aforementioned equation with electric field, $\mathbf{p} = \alpha\mathbf{E}_0$, polarizability then becomes :

$$\alpha = 4\pi\epsilon_0 a^3\frac{\epsilon-\epsilon_0}{\epsilon+2\epsilon_0}. \tag{217}$$

Polarizability demonstrates the response of the material to the electric field when excited. Scattered and absorbed parts are the functions of polarizability. If the denominator goes to zero, maximum resonance is obtained [31]. Cross-section in optics is found by the scattered or absorbed power over the field intensity. The extinction spectrum, which is the sum of scattering and absorption cross-sections is the prime method for examining the plasmon response of a particle, shape and material dependence, etc. Since the scattering cross-section is proportional to the absolute square

of polarizability function, $\sigma_{scatt} \propto a^6$, whereas $\sigma_{abs} \propto a^3$. Thus, as the particle size grows, scattering dominates the plasmon response. Absorption and scattering spectra of spherical metal particles with varying sizes are shown in Figure 2.7 as calculated via numerical methods such as FDTD which will be revisited for the simulation of the substrates in the results chapter.

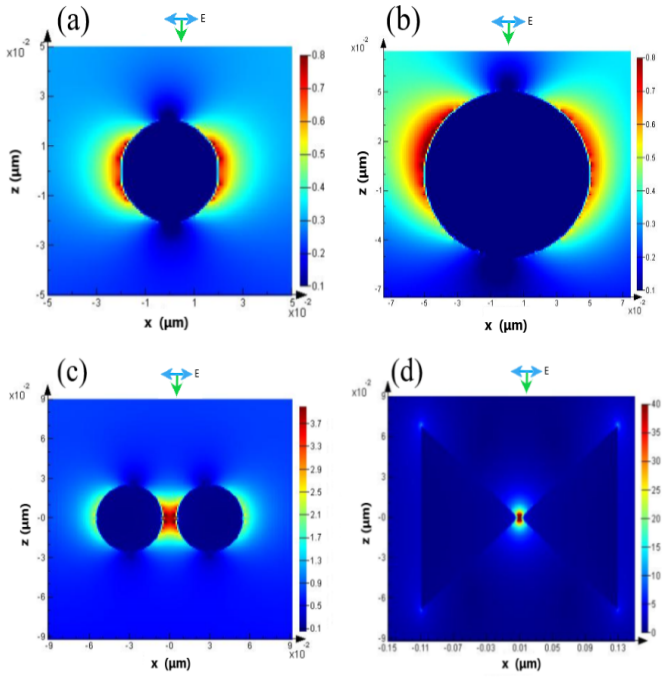

Figure 2.6: Example Finite-Difference-Time-Domain (FDTD) simulations of E-field on the silver nanoparticles with various size and configurations for representing LSPR : a)Ag nanosphere with 40 nm diameter b) Ag nanosphere with 100 nm diameter c) Ag dimer with 50 nm diameter d)Ag bow-tie.

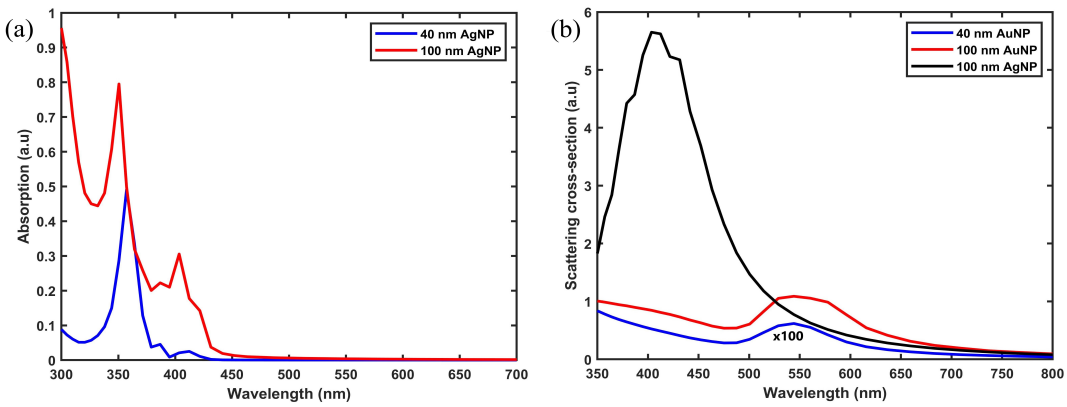

Figure 2.7: FDTD-calculated a) absorption and b) scattering spectra of spherical Ag and Au nanoparticles with 40 and 100 nm diameters.

Spheres that have comparable size with wavelength must be examined through Mie scattering, not in the electrostatic approximation [31, 32, 33]. More complicated geometries need different approaches such as "plasmon hybridization" [34], where two or more metal-dielectric geometries interact with each other such as concentric shells. For more arbitrary and rough structures, numerical methods are required rather than analytical solutions such as Finite-Element Method (FEM), Discrete Dipole Approximation (DDA) and Finite-Difference Time-Domain (FDTD) [35].

2.2 Fabrication Methods : Silicon Surface Nanostructuring

Silicon is one of the most commonly used elements in experimental solid-state physics and photovoltaics as a substrate owing to its abundance, processable and semiconducting features. Crystalline silicon has the diamond cubic crystal structure that consists of FCC lattice with a basis of two silicon atoms. Any type of silicon with different crystalline features and dopants can be used in different parts of solid-state applications. It is highly suitable for laser and chemically induced etching processes. Depending on the dopant, crystal growth, resistivity, and lattice parameter, the crystalline surface can be structured in various morphologies [36].

Surface structuring techniques in micro and nanoscale of crystalline solids are one of the key concepts in solid-state physics and material science applications for sensing,

and photovoltaics, in fact, almost for any device applications in nanotechnology [37]. Advantages of these top-down techniques can be listed as obtaining large surface area, periodic or random structures, rough and highly absorbent surfaces, etc. It is appropriate to divide these methods into dry and wet techniques. Apart from the lithography techniques [17] that require additional layers like photoresists onto the substrate such as photolithography, nanosphere lithography and, interference lithography; electron-beam and focused ion beam (FIB) lithography techniques can directly modify the Si surface. These methods have the precision of a few nanometers however the precision comes with high fabrication costs. An easier way to achieve nanostructuring is applying Laser-Induced-Periodic-Surface-Structures (LIPSS) [38] by directing ultrashort laser pulses to the surface. Laser wavelength and pulse duration change the resulting surfaces however, only periodic surfaces are created. Nanosecond and CW lasers are more suitable for bigger-scale and low-cost structuring. One of the methods that enable morphology variety is etching. Apart from the dry etching techniques such as etching in gaseous environments [39], plasma etching [40], and reactive-ion etching (RIE), we are particularly reviewing the wet chemical etching of silicon. Etching of silicon is possible chemically, electrochemically [16] and photoelectrochemically, photochemically, and metal-assisted [6, 41, 42, 14, 43, 44, 45].

2.2.1 Laser-Assisted Chemical Etching of Crystalline Silicon

The commonly used etchants of the silicon are typically HF for isotropic; NaOH, and KOH for anisotropic etching [36, 41, 42, 14], along with oxidizing agents such as H_2O_2 and HNO_3 that are used with HF. Although the chemical structuring reactions are different in terms of by-products, the general behavior is that one reactant attacks the Si on the solution interface (etching reaction) while another reactant collects electrons (oxidation). In photo-induced etching cases, the incoming photon excites the electron to the conduction band assuming the energy of the photon is equal or greater than the semiconductor bandgap. Another important mechanism is the "band-bending" [46, 6]. When two materials are in contact, in order to facilitate a thermodynamic equilibrium, two Fermi levels would be equalized. The work function of n-type Si is around 3.85 eV, while, for instance, the work function of silver is around 4.5 eV [47]. Then, the band bending becomes upwards from silicon to

silver. The same is applied for the HF solution n-type Si interface, whereas the opposite bending becomes in p-type Si. The band bending scheme determines the carrier motion. As shown in the Figure 2.8, band bending of n-Si and p-Si are compared along with the carrier transitions. Since electrons are excited, remaining holes move through the surface interface in n-Si, which initiate the etching reaction. Conversely, in p-Si, holes move opposite to the illuminated area. The scheme a) also demonstrates another important aspect that, the bandgap broadens towards the etched surface. The role of the oxidant here is important since it collects the electrons by preventing the recombination with the holes. In the chemical aspect of the interface, the etching reaction is photo-initiated on the H terminated Si surface due to HF treatment before the process [48]. Si atoms are dissolved due to the anodic dissolution of Si and cathodic reduction of the oxidant. The overall etching and oxidation take place as follows :

$$Si + 2H_2O_2 + 6HF \rightarrow H_2SiF_6 + 4H_2O \tag{218}$$

Oxidation is the rate-limiting step for aqueous etchants, aqueous etching is not diffusion-limited. Apart from the chemical concentration, laser intensity is one of the key determinants of the resulting micro and nano-holes.[49] The higher the intensity, the more photons excite the surface. Thus, roughening on a large area with higher power can be achieved, or micro-holes on a more focused area can be obtained due to higher intensity.

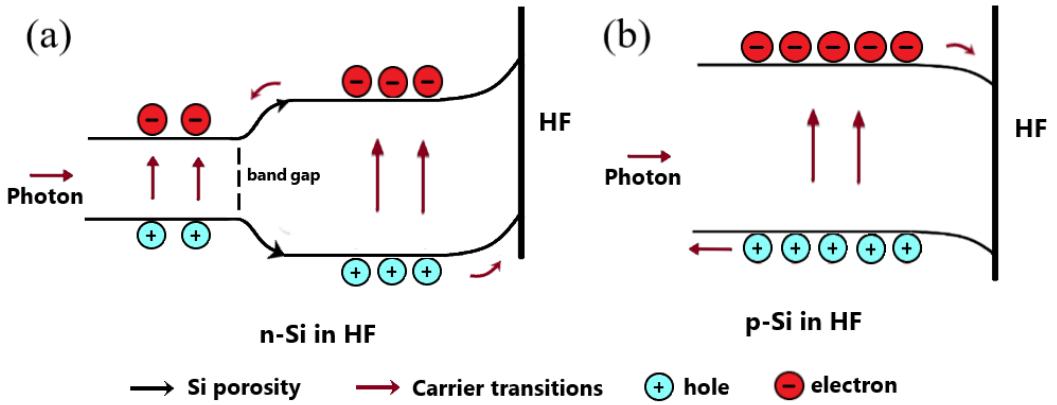

Figure 2.8: The scheme shows the electron and hole transitions in band bending of the interface HF and a)n-Si b)p-Si. Band gap increase in a) is due to increasing silicon porosity. Adopted from the reference [6].

CHAPTER 3

EXPERIMENTAL METHODS

3.1 Photochemical Nanostructuring of Crystalline Silicon

3.1.1 Wet Chemical Stage for Photochemical Etching

Before starting the photochemical etching of silicon, an appropriate silicon wafer is chosen. In these thesis work experiments, n-type P dopant, CZ, 250 μm thickness double-side polished mono-crystalline silicon wafers are used. Si wafers are cleaned in the fully equipped wet bench via standard RCA-1 and RCA-2 cleaning methods in order to remove organic and ionic residues. Before each process, cleaned silicon substrates are immersed in dilute 1:1 hydrofluoric acid (HF 40%) solution for a few minutes for removing oxide layers on the surface and making the sample hydrophobic [48]. Then, the solution required for photochemical etching is prepared. Hydrogen peroxide (H_2O_2 30%) is carefully added to the DI water, and then HF is poured. The solution consist of HF, H_2O_2, and DI water with the concentrations of 10:7:3, respectively. The overall volume of the solution is 100 mL. The etching solution and the silicon wafer pieces are immersed in a Polypropylene container which has plexiglass window for lossless laser beam transmission. No reaction with the solution is observed as the silicon samples are submerged without illumination.

3.1.2 Optical Setup Scheme and Spatial Modulation of Laser

Once the HF solution is prepared and put into the safe plastic container with plexiglass enclosure on top of it, it is illuminated by the CW 532 nm laser beam on the optical setup. The optical setup consist of mirrors and lenses to adjust desirable spot

distance and focus. As seen in the Figure 3.1, before the beam reaches to the samples, it is projected onto the Digital Micromirror Device (DMD) [7] programmed via computer interface. DMD is a type of Spatial Light Modulator (SLM) 0.65 inch screen composed of adjustable 12° tilted around 2 million micromirrors having 1920×1080 resolution. DMD is used in direct laser lithography, 3D printing and adaptive optics. The mirrors are programmed according to the loaded binary images, which constitute the new laser spot size instead of the output beam excited from the laser source itself. The adjusted beam is directed onto the sample of which diameter ranges from approximately 100 μm to 1 cm effectively on the sample. Along with size, duration periodicity can be adjusted by duty cycle features assigning the mirrors to different opening and closing times. The CW laser source itself can be arranged up to 1.5 Watt. However, DMD and other optical components absorb the output power down to few hundreds of mW range.

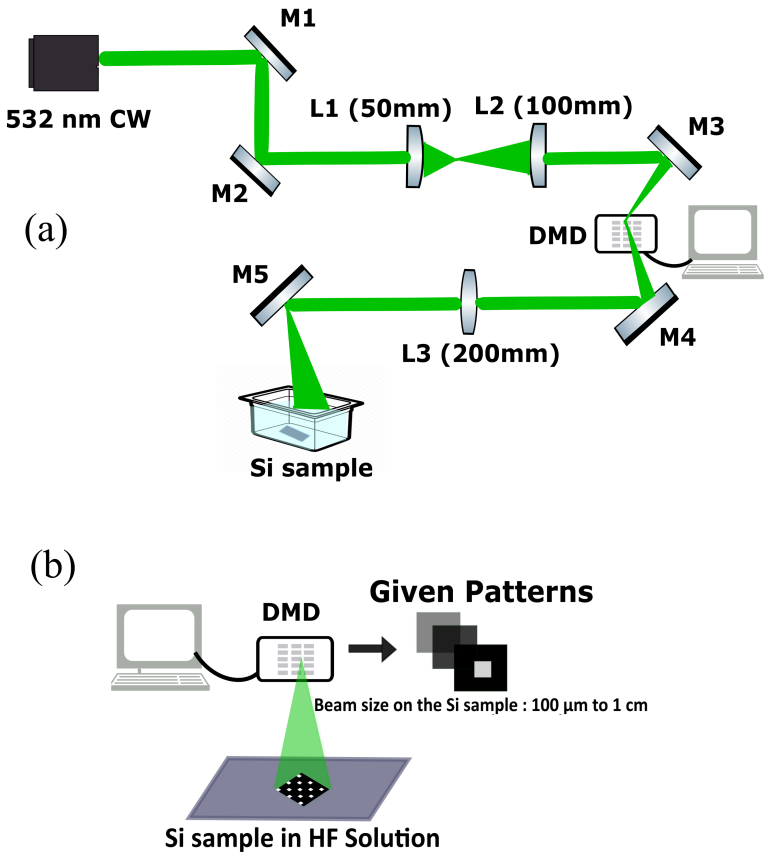

Figure 3.1: a) Experimental setup of LACE with b) spatial modulation of laser beam via DMD [7].

3.2 Fabrication and Characterization of SERS Substrates

3.2.1 Metal Nanoparticle Synthesis on Nanostructured Si

Gold precursor solution for nanoparticle synthesis is prepared using aqueous solution of Tetrachloroauric acid ($HAuCl_4$) whereas silver precursor solution is prepared with aqueous silver nitrate ($AgNO_3$) solution. Solutions are prepared in 1 mM. HF (40%) is added to precursor solutions as 10% of the volume as a reducing agent ensuring the adhesion of metal particles onto the Si surface. Nanostructured Si samples were already cleaned with standard RCA wafer cleaning procedure beforehand for removing organic and metal contamination, then, they are immersed in HF to remove the oxide

layer. Also, glassware is treated with aqua regia in order to remove metal contamination beforehand. Samples are immersed in solution from 30 s. to 5 minutes in silver solution whereas 5-20 minutes required for the gold solution.

3.2.2 Deposition via Thermal Evaporation Technique

The metal deposition technique we use in this work is under the umbrella of physical vapor deposition (PVD) [50], implying that no reaction occurs in the deposition chamber, that is, the target is physically decomposed and deposited onto the substrate. Various methods including RF and DC sputtering, magnetron sputtering, electron beam, and ion beam evaporation, and as employed by us, thermal evaporation deposition are available for substrate coating purposes.

In the thermal evaporation technique, the target to be deposited is placed inside thermal boats that are resistive. Power is supplied via DC power supply up to 1000 W output power. Targets are generally used as pellets, pieces, chunks, wires, etc. As the power is increased from a power supply, the target, e.g silver pellets initially melt, then, evaporate onto the substrate holder in a conical manner. Uniformity or precision control over the deposition can be adjusted by decreasing vacuum level down to high vacuum (HV) levels (e.g 10^{-6} Torr). By doing so, the mean free path becomes compatible with centimeters, which corresponds to the distance between the boat and the sample holder. As the holder rotates in a high vacuum, samples are coated with silver and gold in the desired thickness ranging from 25 nm to 100 nm uniformly in 1 Å/s deposition rate.

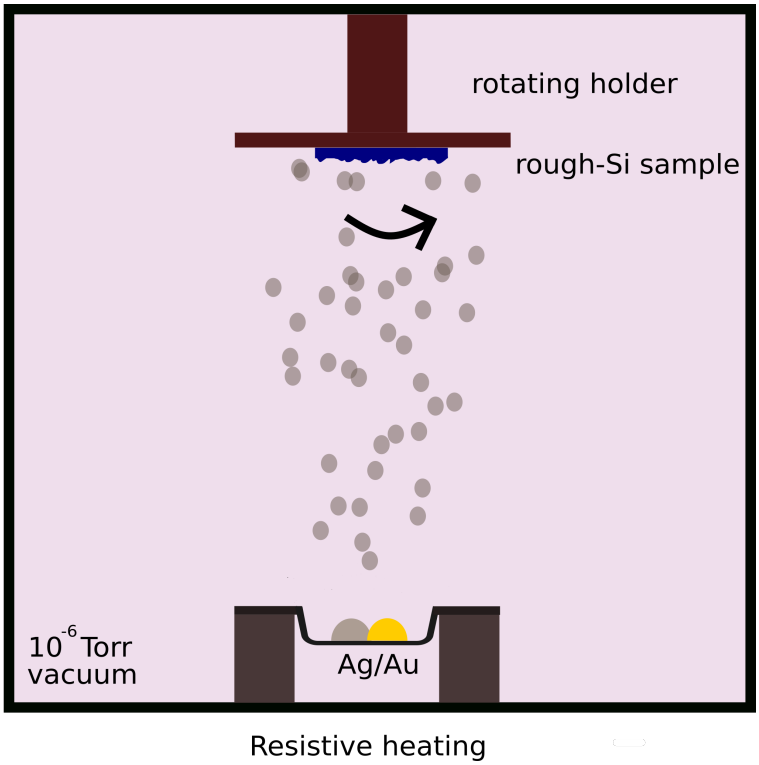

Figure 3.2: Thermal evaporation deposition scheme for silver and gold coating onto photochemically etched Si.

3.2.3 Adsorbing Raman Analyte Molecule

Raman analyte molecules are adsorbed on the substrate surface by utilizing spin-coater for a uniform distribution over the surface. Molecule drops are adsorbed up to 100 μL with 1000 rpm. Analytes are generally adsorbed for one time per substrate only, if needed more, they are absorbed on the ascending order of the molarity after being washed with DI water. The SERS spectra in this work are generally obtained using Brilliant Cresyl Blue (BCB) dye tracer molecule including its limit of detection. BCB is a synthetic chemical obtained as powder and soluble in DI water and ethanol. Its absorption maximum is located around 620 nm. Besides BCB, as a demonstration of the wide range of applicability of the substrates, other common dye molecules such as Crystal Violet (CV), Rhodamine 6G (R6G) are employed [51, 52, 53]. These dyes are also synthetic powders which have absorption maxima at 590 nm and 528 nm, respectively. R6G has also strong fluorescent response emitted around 550 nm.

A critical molecule that is found in fertilizers and explosives like ammonium nitrate (NH_4NO_3) is also examined with various molarities on the fabricated substrates. Corresponding Raman band assignments of the peaks are shown in the next chapter.

3.2.4 Characterization Techniques

The images of the fabricated substrates are obtained via SEM and AFM imaging along with an optical microscope, whereas nanohole densities are analyzed by reflectance and AFM-SEM image analysis tools. Dark field scattering spectra are obtained using a Zeiss Axio Observer inverted microscope with a reflective dark field module and using 100X dark field objective and Ocean Optics Maya spectrometer. The Raman Spectroscopy setup consists of a CW 532 nm laser fiber coupled to a Nikon Eclipse LV100 microscope equipped with a 100X/0.90 NA Nikon objective used in excitation of the sample and collection of the signal and fiber coupled, f/9.8, 750 mm Raman spectrometer (Andor SR750) with 150 l/mm grating and Andor newton EMCCD camera. A schematic figure of Raman setup is shown in Figure 3.3. The exciting laser power on the substrates is 9 mW. In order to compare the measurements with another excitation source, Raman spectra are also acquired using a CW 660 nm laser at the same power. Raman maps are obtained in METU Central Laboratory using a Renishaw InVia confocal Raman microscope with 532 nm laser illumination, 1800 l/mm grating, and a 5X objective.

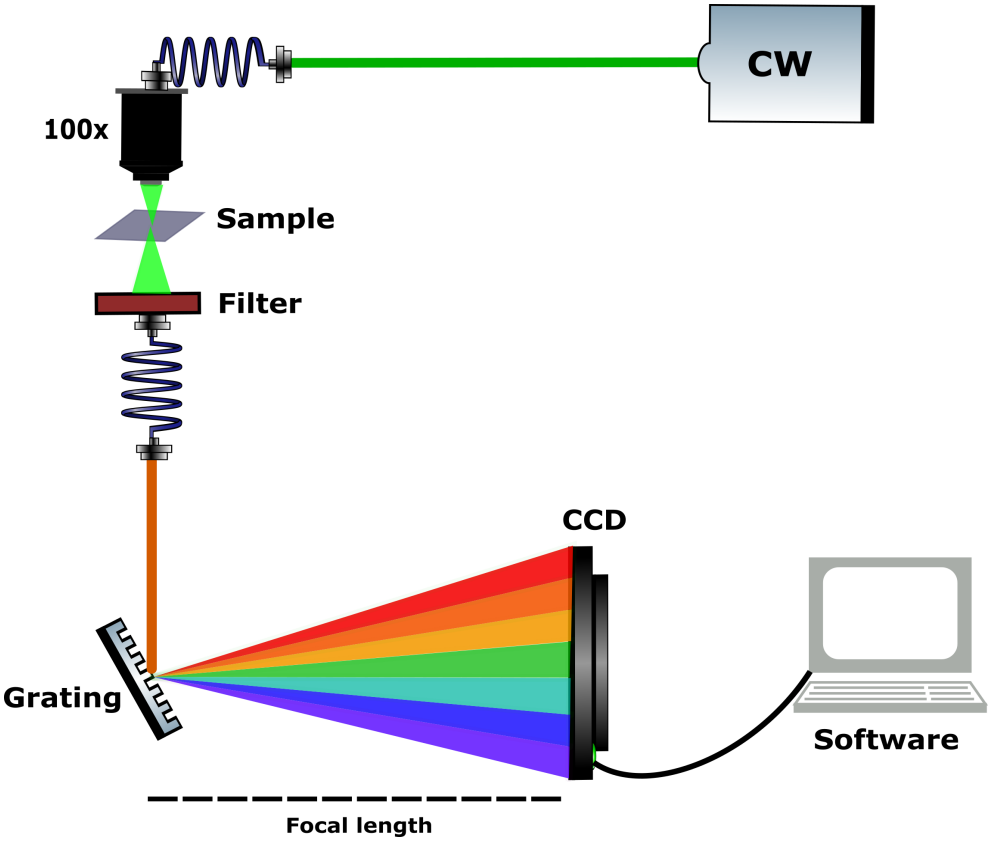

Figure 3.3: Schematic view of Raman spectroscopy used in the experiments. Output of 532 nm linearly polarized CW laser excitation is coupled into the fiber and passes through the objective of a dedicated Raman spectroscopy microscope onto the sample.

CHAPTER 4

RESULTS AND DISCUSSION

4.1 Photochemically Nanostructured Silicon Surfaces

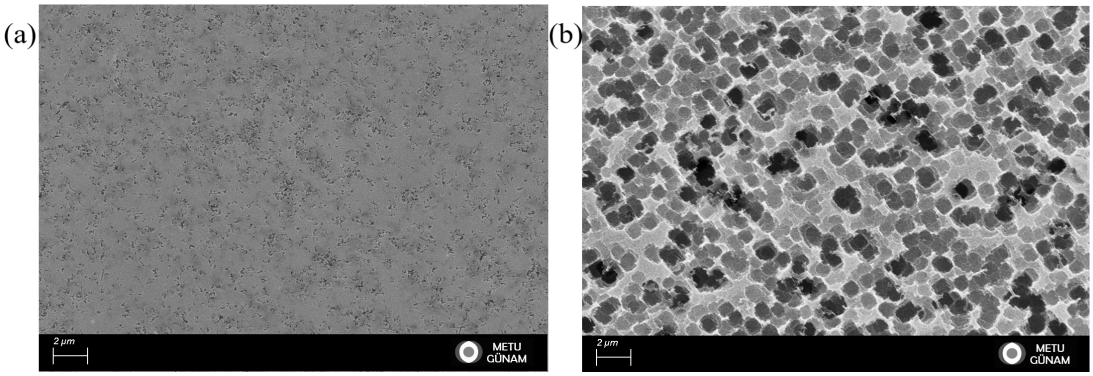

Figure 4.1: SEM images of nanostructured Si surfaces illuminated by intensities a) 0.3 and b) 1.3 W/cm^2.

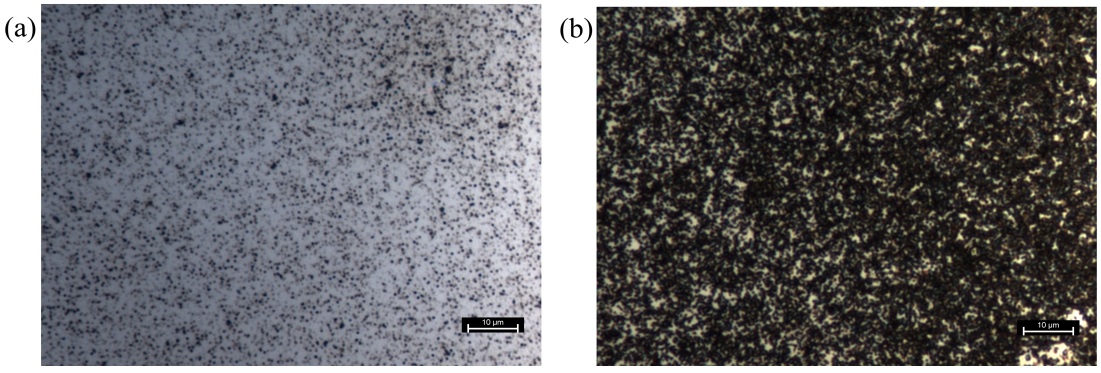

Figure 4.2: Optical microscope images of nanostructured Si surfaces with about 40% and 90% of nanohole surface coverage with 5 minutes and 15 minutes of etching duration.

Before demonstrating the effect of silicon surface structuring on SERS spectra as a function of etching parameters, it is more plausible to show the characterization of structured Si itself in advance. Then, one would grasp a better visualization of how an etched surface could affect the hot-spot density and shape the plasmon response. More characterization figures are provided also in the substrate performance evaluation section afterward. As reviewed in a general manner in the second chapter, formation of nano-holes are the collective result of the intensity and duration of the irradiation, the concentration of the fluoride, and oxidant proportions that dissolve Si and remove electrons for reaction continuity. The difference in those parameters change not only an individual nano-hole structure, but also significantly affect the overall distribution on the Si surface and sizes of them as in the Figure 4.1 from the SEM image of nanostructured Si. The variations in the surface coverage levels depending on the structuring parameters are also shown in Figure 4.2 from the optical microscope images. Specific effects will be examined in the next section case by case.

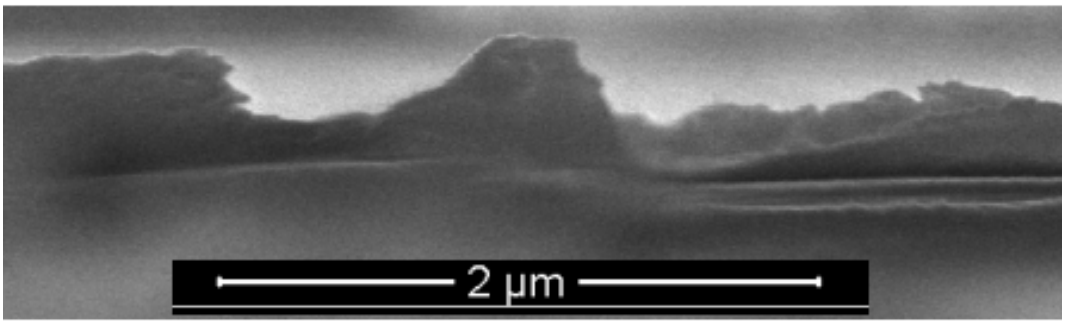

Figure 4.3: Tilted SEM cross-section of an indivdual photochemically etched nano-hole.

Individual nano-hole is shown in the cross-sectional SEM image in Figure 4.3. The depth and hole structure are also parallel to the AFM cross-sectional images in Figure 4.4. From a broad perspective, crystalline structure and macro-scale surface features of silicon are altered due to the formation of roughness. Figure 4.5 a) shows an increase in the intensity of the characteristic Si peak around 520 cm^{-1} in a normal Raman spectrum. As the surface roughness increase, the contribution of the material to a vibrational mode in the spectrum increase due to higher volume. Besides

intensity, it is possible to observe a slight spread in the peak along the wavenumber axis with the increasing roughness. An increase in the full width at half maximum indicates the degradation of the single crystalline structure. In the b) part, reflectance is shown to significantly decrease with roughness. However, the aim here is not to obtain black-Si which is also possible using the same method of photochemical etching. Roughness level and nano-hole sizes should be kept at optimal nanoscale values to ensure the best enhancement. Further increase in nano-hole size and depth as in black Si, may result in a decrease in the enhancement.

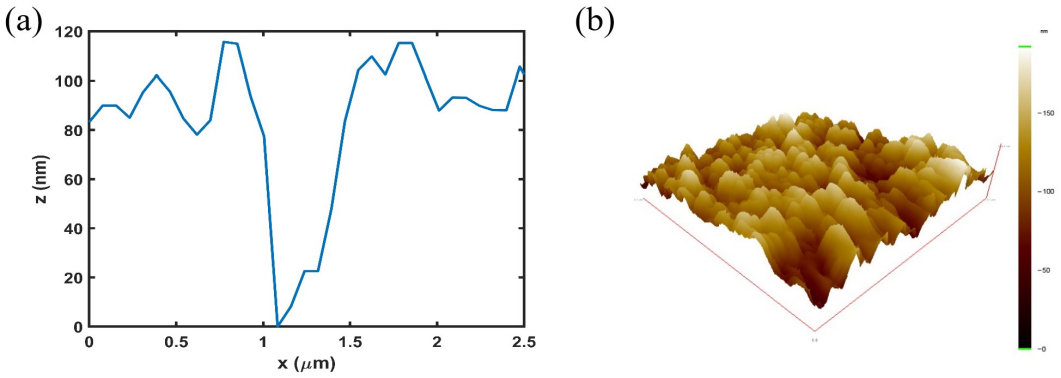

Figure 4.4: a)AFM cross-section of an individual nano-hole from the nanostructured silicon etched under 1.3 W/cm^2 laser intensity. b) 3D equalized AFM image of resulting nanostructured silicon surface.

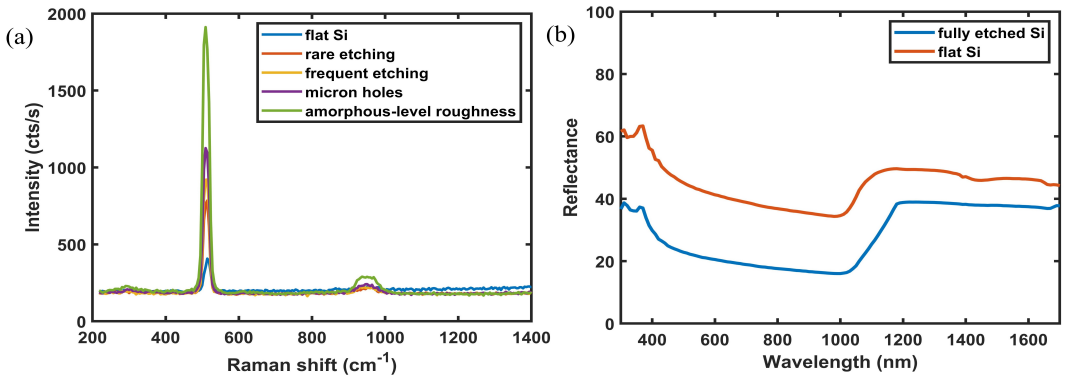

Figure 4.5: a) Normal Raman spectra of Si surface with varying etching levels from 40% of surface coverage up to 90%. b) Reflectance spectra of flat and etched Si surface.

4.2 SERS Measurements via Fabricated Substrates

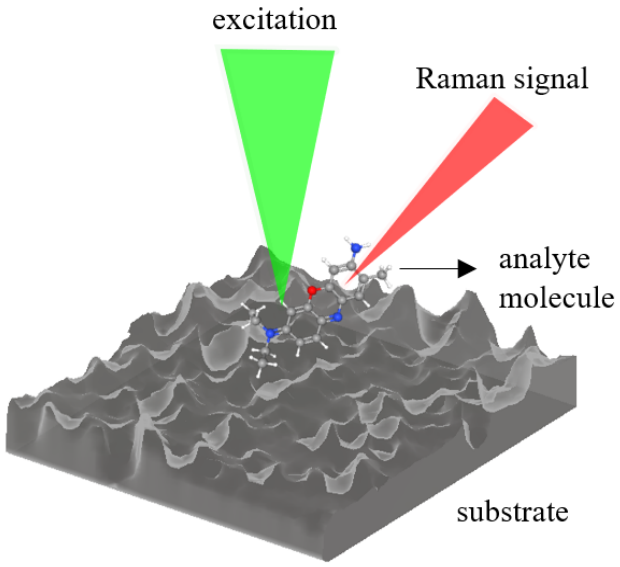

Figure 4.6: Scheme of an example substrate of Ag-on-nanostructured Si and BCB analyte molecule under excitation of Raman spectroscopy.

In this work, roughened silicon surface, more specifically, the nano-holes and ridges within them distributed non-periodically along the surface are the key templates for hot-spot formation. Differences in surface roughness can drastically impact the enhancement that can be observed when deposited with a plasmonic material. A schematic and real examples of fabricated SERS substrates are shown in Figure 4.6 and 4.7, respectively.

In Figure 4.8, 2 different comparative Raman spectra with different nano-hole densities of the same molecule and the deposition are shown. The spectrum in (b) shows a more dramatic change whereas part (a) has a linear increase with increasing nano-hole density. It can originate from the joint effect of both surface structures and metal deposition owing to the non-linear enhancement nature of SERS. In this section, the effect of metal deposition will be kept constant as much as possible to demonstrate the impact that surface structuring parameters can make on the SERS performance. For the process of photochemical etching of crystalline silicon, the main structuring factors are laser-dependent parameters, duration, and solution concentration as mentioned earlier in the chapter.

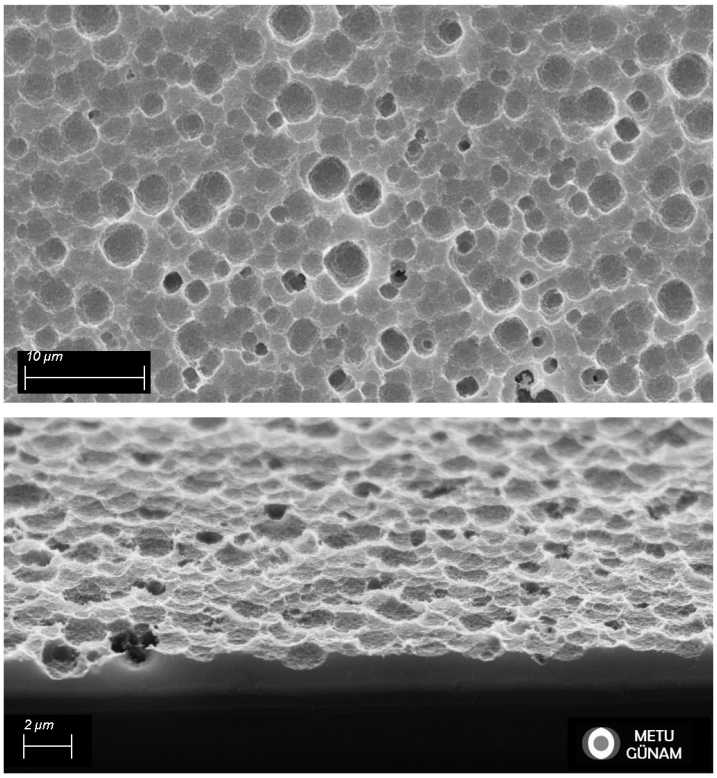

Figure 4.7: SEM images including cross-section of 50 nm Ag deposited Si substrate etched under the laser intensity of 1.3 W/cm^2. This is an example of the most frequently used SERS substrate in this work.

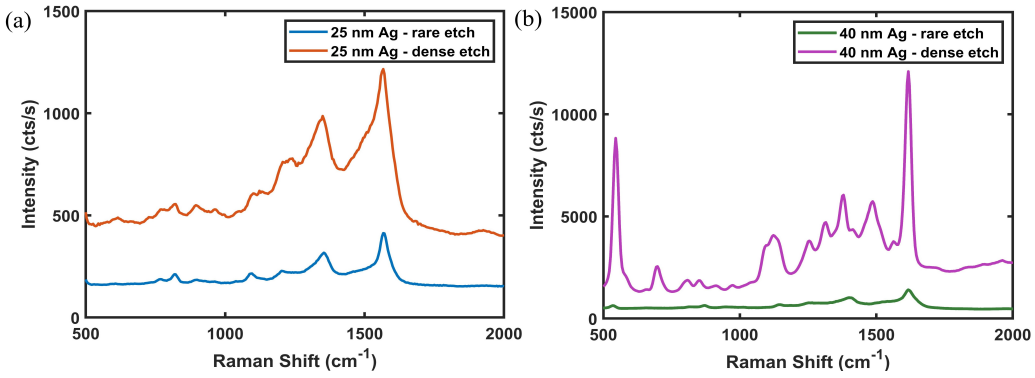

Figure 4.8: Effect of nanohole density demonstrated on 10^{-5} M BCB SERS spectra for the substrates deposited with a) 25 nm Ag b) 40 nm Ag. Rare and dense etching correspond to 40% and 90% nanohole surface coverage.

4.2.0.1 Substrates Nanostructured with Different Concentration Ratios

During the photochemical etching reaction on the silicon and solution interface, HF and H_2O_2 have different roles as explained in the second chapter. Their volume and ratios in the solution can significantly change the resulting nanostructures. If the fluoride concentration is sufficient for the reaction with the silicon all over the surface and the reaction duration, the second determinant concerning the structures is the HF ratio with the oxidizing agent, H_2O_2. With low concentrations of HF, no significant etching reaction and resulting nanostructures are observed. SEM images in Figure 4.9 represents the slow increase in the HF with a constant peroxide volume. Below the 1:3 ratio of HF to H_2O_2, etching did not start. For the low ratios of H_2O_2 however, etching reaction occurs but the resulting density of nanoholes becomes less than with larger concentrations of H_2O_2 as observed in the Figure 4.10.

SERS spectra of the structured Si with 3 different solution ratios in the same thickness and molecule are shown in Figure 4.11. Since the solutions have sufficient amount of the chemicals resulting nano-holes are already frequent and thus SERS spectra deviate not so much. However, the figure shows that the two different extreme ratios do not ensure the most enhancement, an intermediate level of concentrations does. Although peroxide is useful for frequent distribution of the holes, it may also increase the depth so that the hot-spot enhancement may diminish.

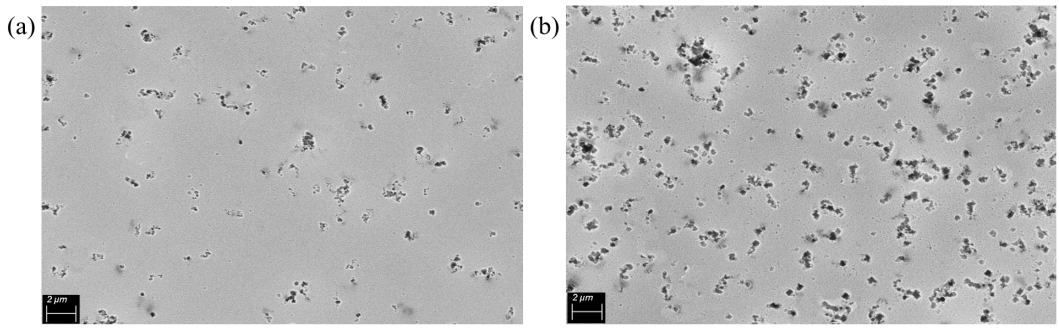

Figure 4.9: SEM images of Si samples immmersed in different solutions with respect to increasing HF ratio from a) to b). a) represents the initial formation of nanoholes in a meaningful density.

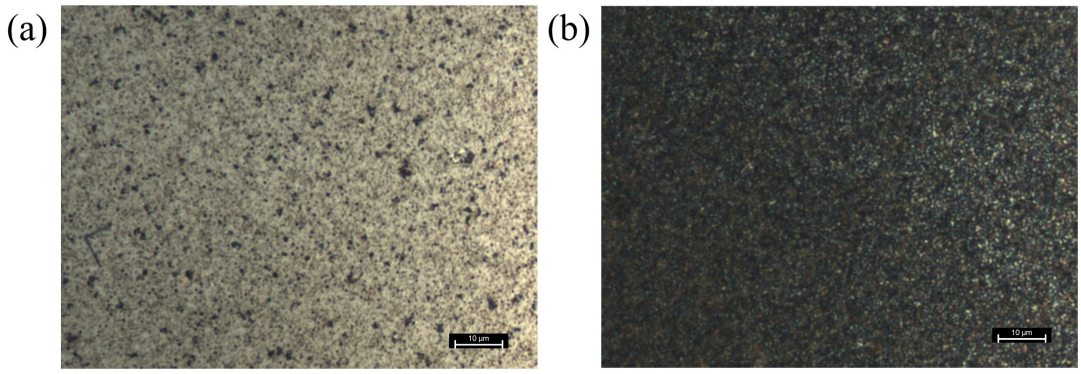

Figure 4.10: Optical microscope images of two nanostructured silicon samples of which photochemical etching solutions consist of a) 2:1 HF:H_2O_2 and b) 1:2 HF:H_2O_2 ratios.

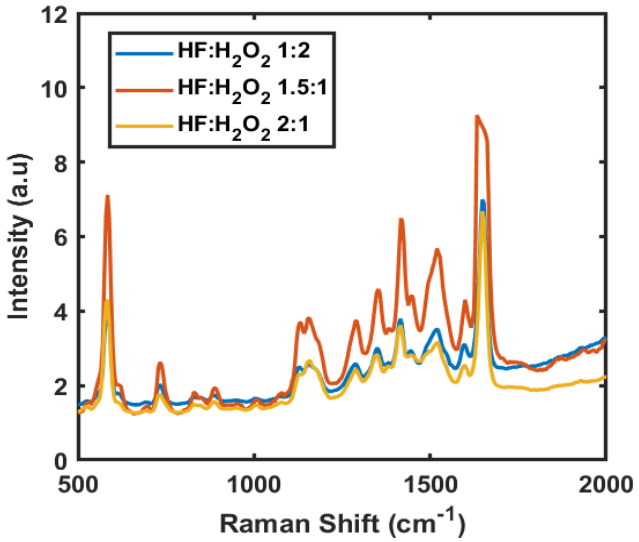

Figure 4.11: Change in the SERS spectra for different etchant and oxidant rations in the same total volume, silver thickness and analyte molarity.

4.2.0.2 Substrates Nanostructured with Different Illumination Times and Periodicities

As the photons impinge on the Si surface and HF solution-Si interface, dissolving of Si and oxidation reactions are initiated. In these specific ratios of solution concentration and volume along with large spot sizes aiming the large area substrate fabrication,

the Si etching rate is observed to be around 1-3 Å/s. Silicon surface becomes considerably rough for SERS application as of 5 minutes of illumination achieving around 100 nm depths for 10-15 minutes. There is no constant increase of depth or nanohole distribution in time as the reaction dynamics change. Rather, the roughness level reaches its optimal level for SERS enhancement around 10-15 minutes as shown in the bar graphs of Figure 4.28.

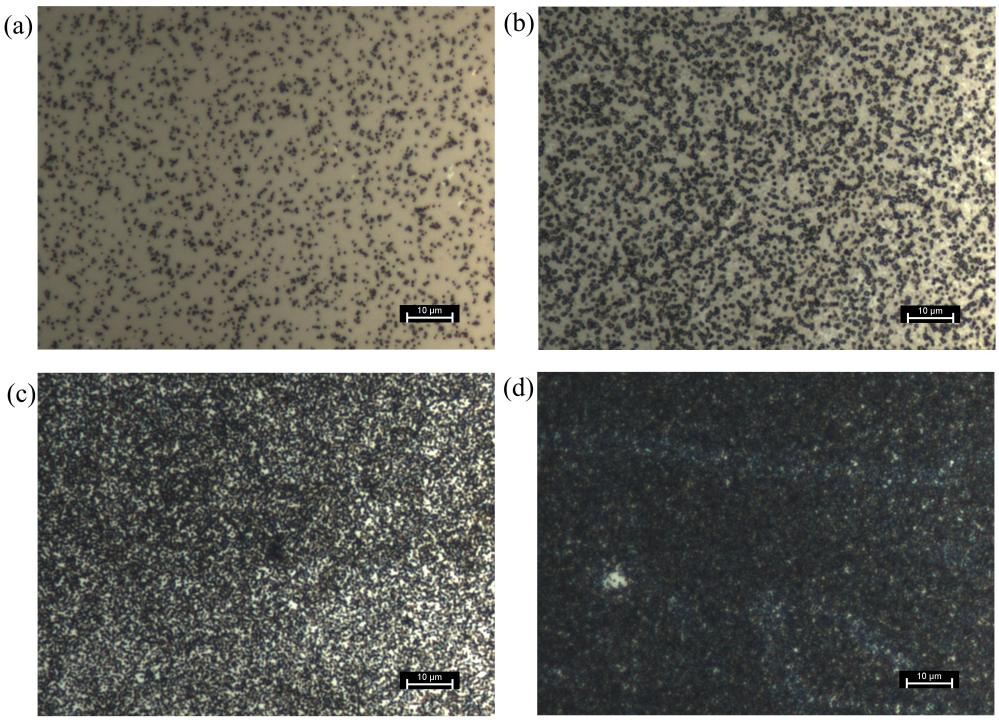

Figure 4.12: Etched Si surface illuminated with a) 100% b)70% c)50% d)30% duty cycles assigned via DMD keeping the total illuminated duration and laser power constant.

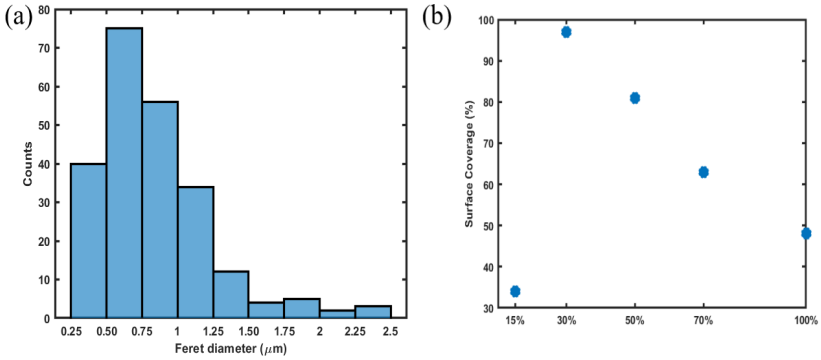

Figure 4.13: a) Feret diameter distribution of resulting nano-holes under 70% duty cycle illumination. b) Surface coverage percentage of Si surface with changing duty cycles.

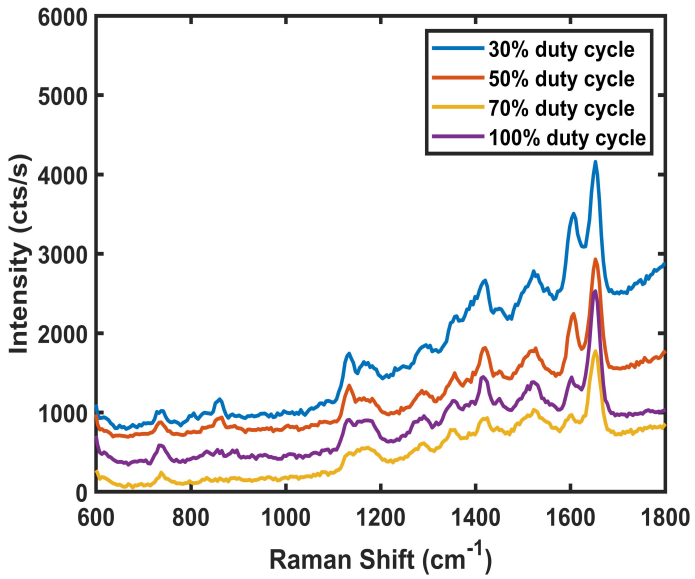

Figure 4.14: SERS spectra of 10^{-5} M BCB on the 50 nm Ag coated Si samples of which surfaces are illuminated with a) 100% b)70% c)50% and d)30% duty cycles assigned via DMD keeping the total illuminated duration and laser power constant in 5 minutes.

Apart from constant illumination on the sample, laser is spatially modulated via DMD such that short breaks on irradiation could be assigned as duty cycles. Even though having total illumination with the same duration such as 5 minutes, as the duty cycles change, resulting hole distribution and width are altered. Because, the dissolving

of Si still continues during the break between the two pulses. Note that referred pulses do not make the laser as a pulse laser since these pulses are on the order of milliseconds. As shown in Figure 4.12, 50% and 30% duty cycles form the most intense distribution since the overall reaction duration increase at least twice by the non-illuminated times, whereas 70% duty cycle forms the most wide nano-holes in that configuration. Resulting hole widths are calculated for 70% duty cycle while for a general picture, surface coverage of Si with nano-holes are calculated with varying cycles as shown in Figure 4.13. Nano-hole density is observed to increase inversely proportional to the duty cycle, however, that is not the case for lower cycles such as 15%. In Figure 4.14, parallel to the nano-hole densities demonstrated in microscope images, 30% duty cycle exhibits higher enhancement than the bigger cycles. As a side note, that may not be the case in the absence of sufficient amount of solution and laser intensity. In that case, cycles smaller than 50% tend to decrease in surface coverage of the holes.

4.2.0.3 Substrates Nanostructured with Different Illumination Spot Size and Output Power

Another critical point to ignite the etching reaction is the illumination power. In this fabrication process, CW laser with a 532 nm wavelength has the output power of up to 1 W . However due to optical loss after DMD and components, maximum 300 mW is obtained. As 50 mW and more power reaching the sample container, a significant etching rate is observed. Power is notably impactful over the nano-hole density and higher powers enable us to have worthwhile substrates in a short period such as 5-15 minutes. However, it does not increase the roughness and sustain the reaction after certain levels and needs to be optimized. The effect of power on the SERS enhancement is shown in the first section of Figure 4.28. 200 mW shows the optimum enhancement by keeping the other parameters constant.

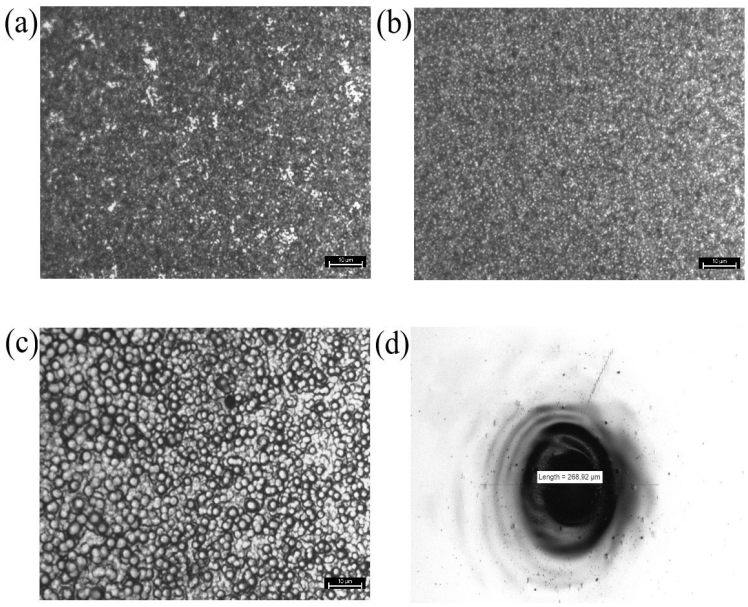

Figure 4.15: Illumination spot size versus resulting holes formed on the nanostructured Si samples : a) 10 mm. b) 5 mm. c) 1.5 mm and d) 0.1 mm as the smallest spot projected onto the sample in the current experimental configuration corresponding to the intensity levels of 0.3, 1.3, 15, and 3333 W/cm^2, respectively.

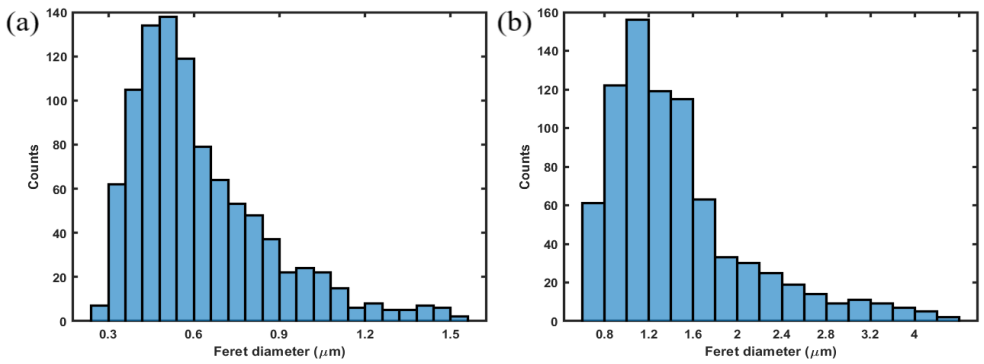

Figure 4.16: Feret diameter distribution of resulting nano-holes illuminated by beam spot sizes with 5 mm and 1.5 mm corresponding to 1.3 and 15 W/cm^2 intensity. Distribution calculations are based on SEM and optical microscope images composed distinctive holes.

Besides adjusting power output, patterns with varying sizes are assigned from DMD in order to compare the effect of spot size, which implies the varying intensities,

on the nanostructures and SERS enhancement. The minimum spot diameter that is directed to the sample is around $80\ \mu m$ however, as the intensity increase due to decreasing area, holes start to become in the micron scale with large depths as shown in Table 4.1 along with the etching rates. Maximum intensity levels due to the smallest spot with 1 W output power corresponds to values up to 10 kW/cm^2 but approximately 300 mW reaches the samples due to losses. With such intensity, we would obtain larger micron-scale structures, however, those structures cannot induce a near field enhancement for SERS as a homogeneous distribution of holes that fills the 100X objective of Raman spectrum setup. Thus, smaller intensity levels resulting in smaller nanoholes are applied for SERS while balancing the dense distribution. Figure 4.28 and Figure 4.15 show effect of spot size on SERS enhancement and resulting Si structures by four different spot sizes with diameters of 0.1 mm, 1.5 mm 5 mm and 10 mm. Intensity levels correspond to 3333 W/cm^2, 15 W/cm^2, 1.3 W/cm^2 and 0.3 W/cm^2, respectively. The optical microscope images in 4.15 show that the holes widen up to microns as the laser intensity increases. The optimum enhancement is obtained for the 5 mm diameter spot size, having around 300-500 nm wide nanoholes and dense distribution. Si hole width distributions are shown in Figure 4.16 as Feret diameters. Obviously, bigger structures due to increasing intensity affect the distribution and shift the overall hole populations to larger widths. However, larger hole widths tend to diminish SERS enhancement due to widening of the hot-spots. Also resulting surface coverage of Si surface with nano-holes is calculated as shown in Figure 4.17 with varying powers for the same spot size.

Table 4.1: Comparative table for varying intensities due to different spot size under the same output power of 0.3 W. Etching rates are calculated based on resulting approximate silicon hole depths and 10 minutes of etching duration.

Intensity (W/cm^2)	Spot Size (mm)	Hole Depth (nm)	Etching Rate (Å/s)
0.3	10	60-80	~ 1
1.3	5	100-120	~ 2
15	1.5	700-800	~ 13
3333	0.1	6000	~ 100

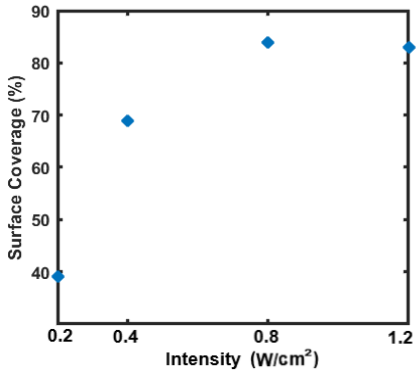

Figure 4.17: Effect of laser intensity on the Si nanohole surface coverage due to increasing power.

4.2.1 SERS Enhancement Dependence on Metal and Deposition Thickness

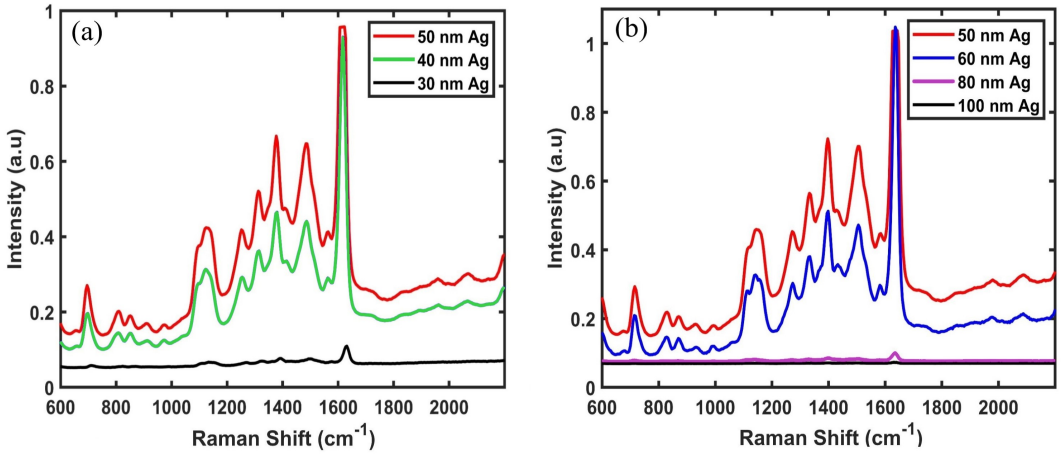

Figure 4.18: a) and b) represents the silver deposition thickness dependence of the SERS enhancement of the substrates fabricated under the same Si nanostructuring parameters such as laser intensity of 1.3 W/cm^2 for 15 minutes.

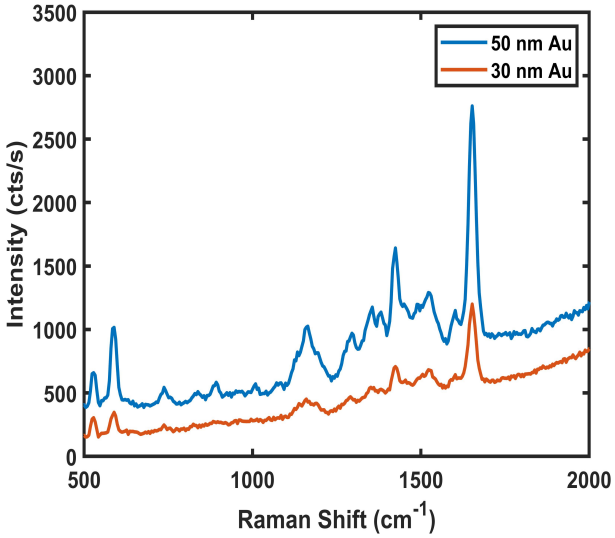

Figure 4.19: Deposited gold thickness comparison of the SERS spectra of BCB with the substrates fabricated under the same Si nanostructuring parameters such as laser intensity of 1.3 W/cm^2 for 15 minutes.

One of the main keystones in this thesis work is to study the contribution of metal film to the enhancement. The choice of the metal changes plasmon response in the spectral range due to differing material properties, but also, metal particle size greatly affects the scattering component. Generally growing size red-shifts the plasmon response, also broadens spectral range of the scattering cross-section. In this case, the particle size corresponds to the deposition thickness provided that the Si surface structuring parameters remain the same for comparison. Figure 4.18 (a) and (b) demonstrates that optimum silver deposition thickness is 50 nm in terms of enhancement performance for that particular photochemically etched Si nanostructures. Si parameters are also chosen to be optimized in terms of nano-hole density. Below and above 50 nm Ag, enhancement significantly drops due to less surface coverage for below 50 nm, and diminishing of hot-spots by covering the nano-holes completely for above 50 nm. The similar trend is observed in Figure 4.19 by depositing Au film onto the same nanostructured substrates.

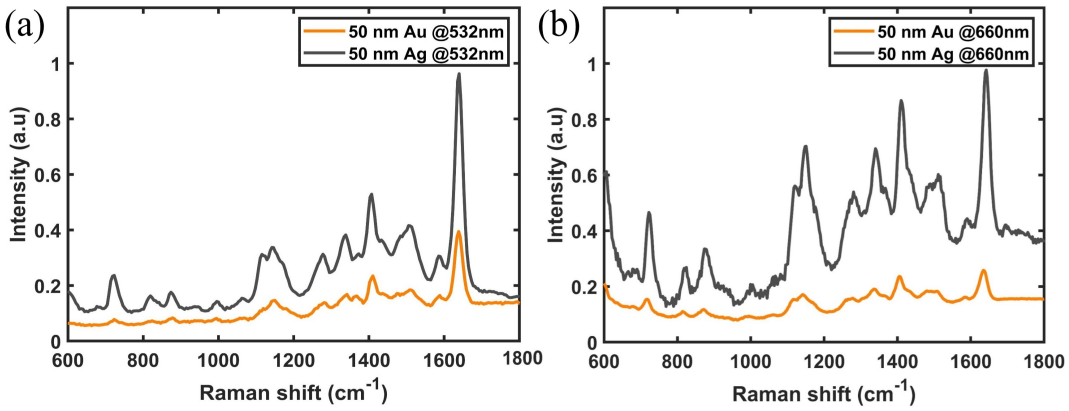

Figure 4.20: SERS spectra of 10^{-5} M BCB adsorbed on 50 nm gold and silver deposited nanostructured Si substrates under 532 and 660 nm Raman excitations.

Figure 4.20 shows an interesting result that will be further revisited in the next sections that 50 nm Ag and Au substrates are examined under 532 nm and 660 nm Raman excitation sources. For the particular Ag and Au on the nanostructured Si substrates, Ag coated structures exhibit better resolved peaks and enhancement than Au coated substrates even under the 660 nm. In order to obtain a larger response under 660 nm, structures can be tuned in size and shape, while also, different Raman probe molecules may have enhanced better under different excitations depending on the vibrational modes.

4.2.2 Nanoparticle Decorated Nanostructured Substrates

Silver nanoparticles are formed on structured Si surfaces using the procedure as mentioned in experimental methods. The Si samples are immersed in the same precursor solution for each measurement. First, Si wafers textured with the same parameters are held in silver nitrate solution with different duration; 30 seconds, 1 minute and 2 minutes. In Figure 4.21, Raman spectra of BCB is measured on those substrates and 1 minute of immersion found to yield the optimal enhancement for such textured Si samples. 1 minute of immersion has more surface coverage than 30 second while keeping the surface roughness. 2 minutes of immersion, despite being more densely packed, overshadows the textured part compared to 1 minute and 30 seconds immer-

sion cases. This part closely resembles the analysis of Ag film thickness spectra, where 50 nm Ag is found to be the optimal thickness for such substrates.

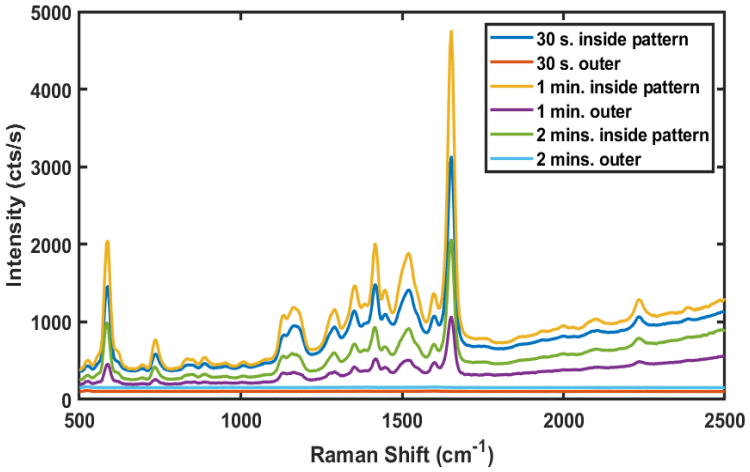

Figure 4.21: SERS spectra of 10^{-5} M BCB adsorbed on silver nitrate solution based textured Si substrates with different immersion times : 30s., 1 minute and 2 minutes.

In Figure 4.22, spectra is obtained from the same silver nitrate solution and immersion times by using different texturing parameters. As expected, the most frequently etched substrate yields more enhancement in BCB spectrum. Similar procedure is repeated for the immersion into the gold precursor solution of structured Si. Having the same molarity with Ag precursor solution, samples are immersed from 10 to 20 minutes for a meaningful formation of AuNPs on the samples. In this case, 10-15 minutes of immersion yields an optimal result for the enhancement of BCB as shown in Figure 4.23. As also shown in the comparative SEM images of AgNP deposited flat and textured Si regions in Figure 4.24, inside the textured area is always advantageous for higher degrees of enhancement due to availability of potential hot-spots whether deposited with silver or gold.

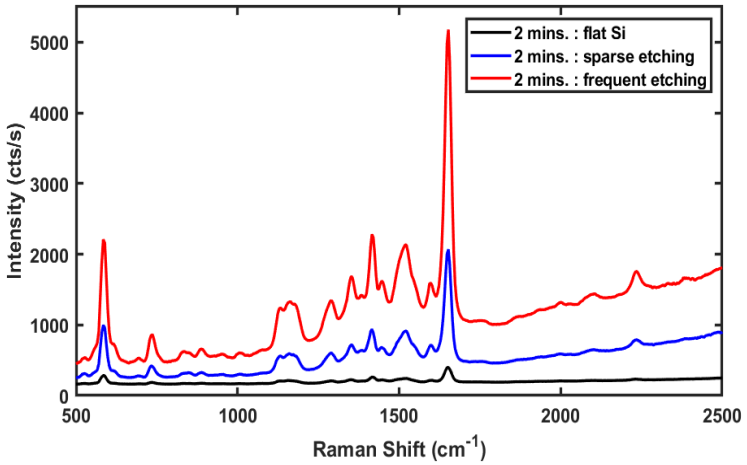

Figure 4.22: SERS spectra of 10^{-5} M BCB adsorbed on silver nitrate solution based textured Si substrates with different etching rates, i.e. 0%, 40%, and 90% of nanohole surface coverage.

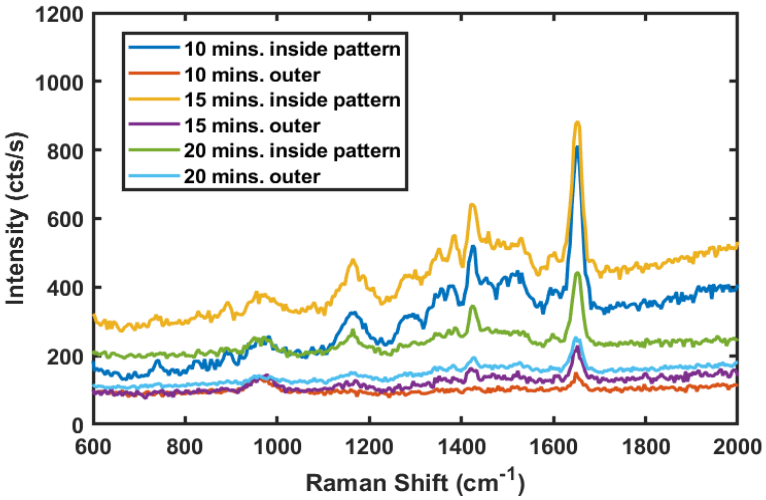

Figure 4.23: SERS spectra of 10^{-5} M BCB adsorbed on tetrachloroauric acid ($HAuCl_4$) solution based textured Si substrates with different immersion times.

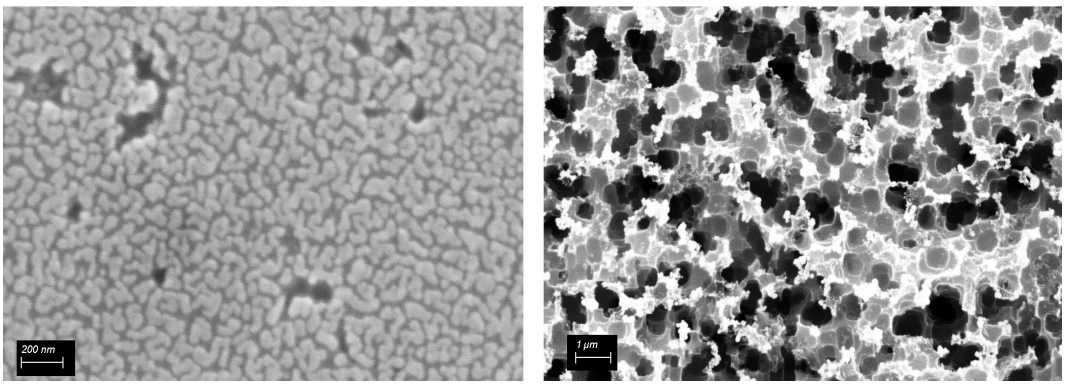

Figure 4.24: SEM images showing AgNPs deposited on flat (left) and nanostructured Si (right) samples.

4.3 Substrate Enhancement Performance Evaluation : Experimental and Numerical Considerations

In the literature, there is more than one SERS enhancement formulation to evaluate the performance of the substrates most of which are still debated whether they overestimate the results or not [54, 55]. It is more challenging to rely on the same formula for different substrates fabricated with different methods such as top-down nanostructured versus adsorbing colloidal particles and analyte onto the flat substrate. A widely accepted experimental enhancement factor calculation is based on the calculation of the number of analyte molecules as shown in the equation below.

$$EF = \frac{I_{SERS}}{I_{Raman}} \times \frac{N_{Raman}}{N_{SERS}} \tag{41}$$

Calculation of EF by picking the characteristic peak area indicated as Raman and SERS intensity in the EF equation. Here, the calculated peak around 1653 cm^{-1} is assigned to the Raman band of symmetrical in-plane C-C stretching. The enhancement factor calculation uses the notion of the number of the adsorbed analyte molecule indicated as N_{Raman} and N_{SERS} [56]. In Table 4.2, calculated approximate EF values of various substrates are based on the reference BCB measurements of 10^{-2} M as N_{Raman} and I_{Raman}.In normal Raman spectroscopy (NRS) inside liquid samples, the 3D Raman probe volume can be determined by considering a prolate spheroid focal

volume, which in our case have dimensions of $r_x = 8.5\ \mu m$, $r_y = 8.5\ \mu m$ and the depth of focus $r_z = 17\ \mu m$, yielding $V_{probe} = (\frac{4\pi}{3}) \times 8.5\ \mu m \times 8.5\ \mu m \times 17 \mu m = 5144.88\ \mu m^3 = 5.14 \times 10^{-12} L$ of probe volume. For our 10^{-2} M BCB solution, the total number of molecules, namely, $N_{NRS} = C_{NRS} \times V_{probe}$, in the measurement volume can be found as $N_{NRS} = 10^{-2} mol\ L^{-1} \times 6.02 \times 10^{23}\ molecules\, mol^{-1} \times 5.14 \times 10^{-12} L = 3.09 \times 10^{10}$ molecules. After baseline correction, I_{NRS} is calculated through the area under the characteristic peak $1653\ cm^{-1}$ is found as 2500 $cts\, s^{-1}$.

Surface area of the structures obtained from the simulation environment is $281.31 \mu m^2$. Molecules in the near field enlarge up to 2 nm from the surface of the metal film, we deliberately exaggerate this value as 5 nm in order not to to overestimate the EF value, resulting in a probe volume of $V_{probe} = 281.31\ \mu m^2 \times 0.005\ \mu m = 1.41 \times 10^{-15} L$. Therefore, the total number of BCB molecules in the SERS measurement can be calculated as $N_{SERS} = 10^{-5} mol\ L^{-1} \times 6.02 \times 10^{23}\ molecules\, mol^{-1} \times 1.41 \times 10^{-15} L = 8.49 \times 10^3$ molecules. The EF is calculated with the measured I_{NRS} and I_{SERS} values as $EF = \frac{I_{SERS}}{2500} \times \frac{3.09 \times 10^{10}}{8.49 \times 10^3}$.

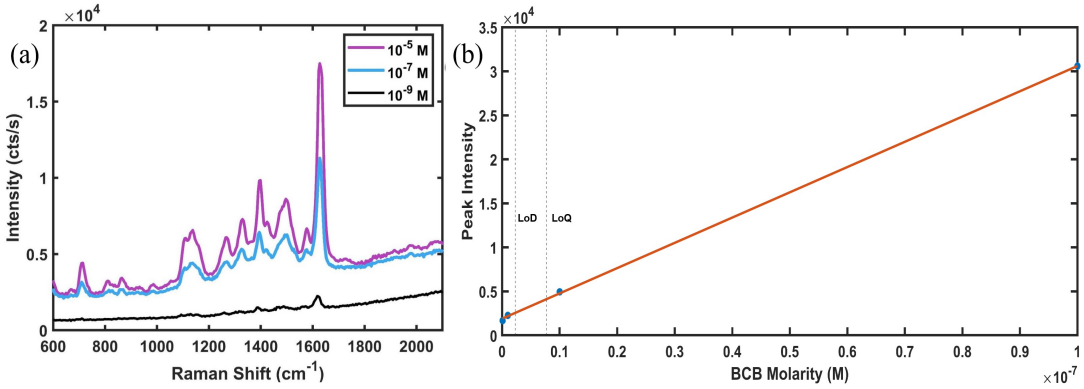

Figure 4.25: a) and b) represent the limit of detection (LoD) and limit of quantification (LoQ) study on the 50 nm Ag deposited substrate. LoD and LoQ are calculated as 2.3×10^{-9} M and 7.7×10^{-9} M, respectively.

SERS substrates can also be evaluated by their detection limit of a molecule. By analyzing meaningful peak levels compared to a noisy signal, BCB is found to exhibit its peaks down to nM orders as shown in Figure 4.25. The 50 nm Ag deposited substrates with the highest nanohole coverage (90%) are used for the detection stud-

ies. Limit of detection and quantification (LoD and LoQ) are calculated with respect to the deviation from the linear regression model in the calibration curve for BCB molecule. LoD signifies the least reliably measured concentration of which signal is distinguished from the noise, while LoQ signifies the least concentration that can be observed accurately and repeatedly [57]. As a result, LoD and LoQ are found as 2.3×10^{-9} M and 7.7×10^{-9} M, respectively. Moreover, a few more fluorescent dyes such as R6G and CV showed strong peaks with moderately low concentrations. A significant material used in explosives and fertilizers, which is ammonium nitrate (NH_4NO_3) is evaluated with the same substrates. SERS measurements compared to their normal Raman spectra are shown in Figure 4.26. The resulting Raman peak assignments are made in Table 4.3. C-C stretching mode in 1653 cm^{-1} and C-C bending mode in 584 cm^{-1} are used to characterize BCB molecule. N-phenyl stretching in 1370 cm^{-1} is attributed to CV and C-O-C stretching in 1270 is assigned to R6G etc. One last experimental analysis is made to compare the homogeneity of the enhancement over the nanostructured area, and the effect of nanostructures itself directly on the enhancement. Although it is shown by various Raman spectra, a mapping is also obtained from a transition region from a photochemically processed area and unilluminated area shown in Figure 4.27. The map shows no significant peak intensity in non-illuminated part, thus, the laser illumination parameters are the key factor for SERS enhancement itself and keeping the homogeneity of the substrate.

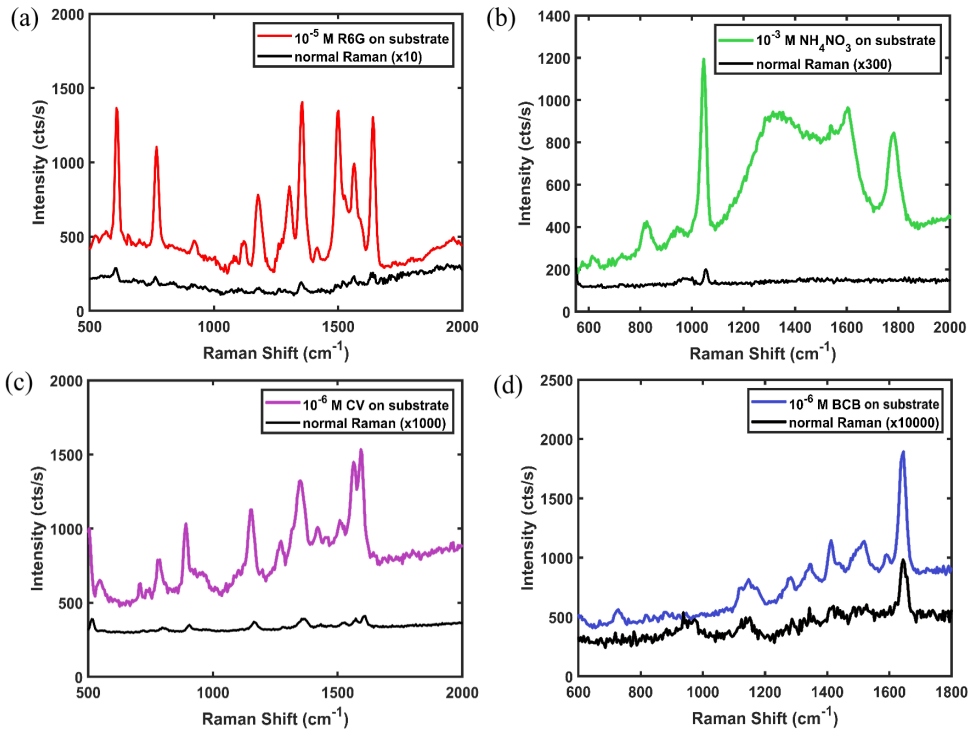

Figure 4.26: SERS and normal Raman spectra comparison of a) 10^{-5} M R6G b) 10^{-3} M NH_4NO_3 c) 10^{-6} M CV and d) 10^{-6} M BCB absorbed on the similar 50 nm Ag coated substrates examined under 532 nm irradiation.

Table 4.2: Calculated EF values of the substrates fabricated using various parameters based on analyte molecule BCB peak at 1653 cm^{-1}.

Substrate Etching Parameters	Deposition	EF
200 mW - 15 minutes - 5 mm	50 nm Ag	$\sim 3 \times 10^9$
200 mW - 15 minutes - 5 mm	30 nm Ag	$\sim 4 \times 10^8$
100 mW - 15 minutes - 5 mm	50 nm Ag	$\sim 1 \times 10^9$
200 mW - 15 minutes - 5 mm	80 nm Ag	$\sim 9 \times 10^7$
200 mW - 15 minutes - 5 mm	50 nm Au	$\sim 5 \times 10^8$
200 mW - 10 minutes - 5 mm	30 nm Au	$\sim 2.6 \times 10^7$
200 mW - 5 minutes - 5 mm - 30% cycle	50 nm Ag	$\sim 1 \times 10^8$
200 mW - 5 minutes - 5 mm - 50% cycle	50 nm Ag	$\sim 5 \times 10^7$
200 mW - 5 minutes - 5 mm - 70% cycle	50 nm Ag	$\sim 4 \times 10^7$
200 mW - 5 minutes - 5 mm - 100% cycle	50 nm Ag	$\sim 7 \times 10^7$
200 mW - 10 minutes - 5 mm	1 min. of $AgNO_3$	$\sim 2 \times 10^8$
200 mW - 10 minutes - 5 mm	10 mins. of $HAuCl_4$	$\sim 1.5 \times 10^7$

Table 4.3: Raman band assignments of Raman spectra of different molecules.Bands at 1653 and 584 cm^{-1} are used for enhancement characterization of BCB [1]. Some bands are common among the dye molecules such as R6G, CV and BCB [2, 3, 4].

Wavenumber (cm^{-1})	Band Assignment
520	Crystalline Si
584	aromatic C-C bending
770	out-of plane C-H bending
1045	N-O Symmetric stretching
1120	in-plane C-H bending
1270	C-O-C stretching
1370	N-phenyl stretching
1570	C-C stretching
1653	C-C stretching

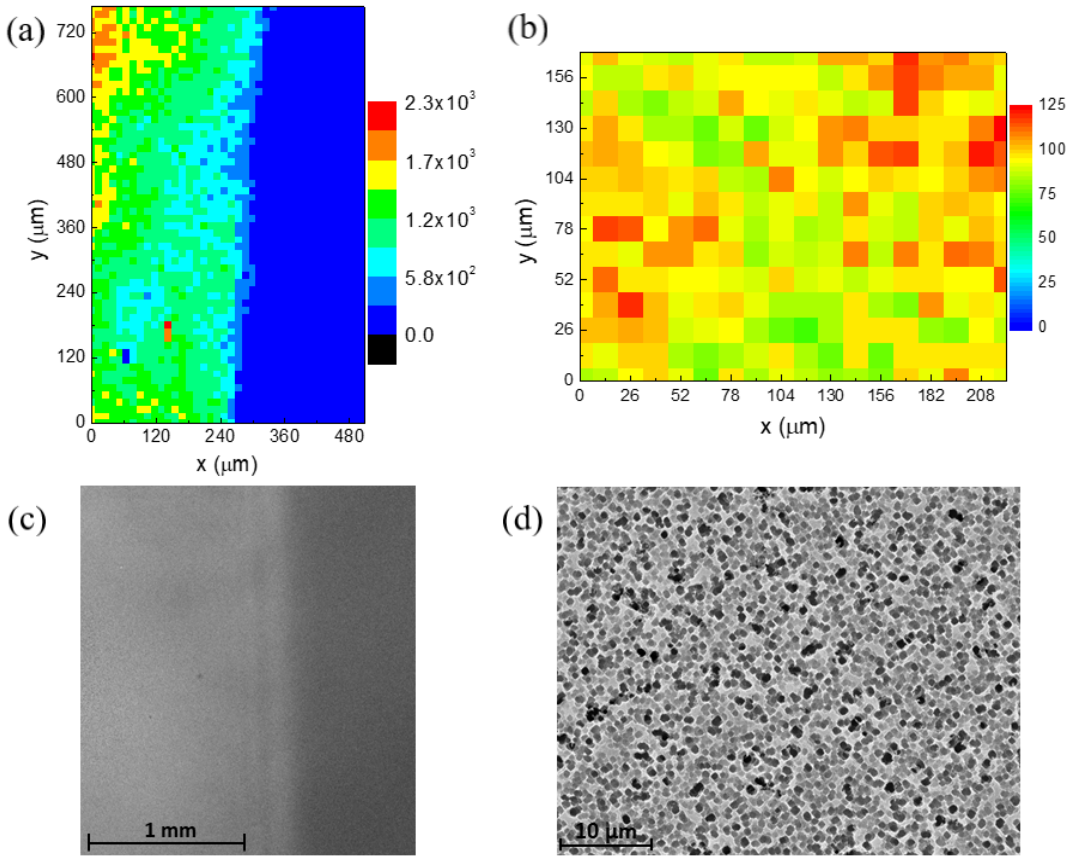

Figure 4.27: a) Raman mapping of a 10^{-5} M BCB absorbed on the transition region throughout the substrate from illuminated part to non-illuminated area. b) The same raman mapping of the textured area. c) and d) represent the corresponding SEM images of the Raman mappings above. The Relative Standard Deviation (RSD) values of the mapping showing the inner textured regions of the substrates are around 20%.

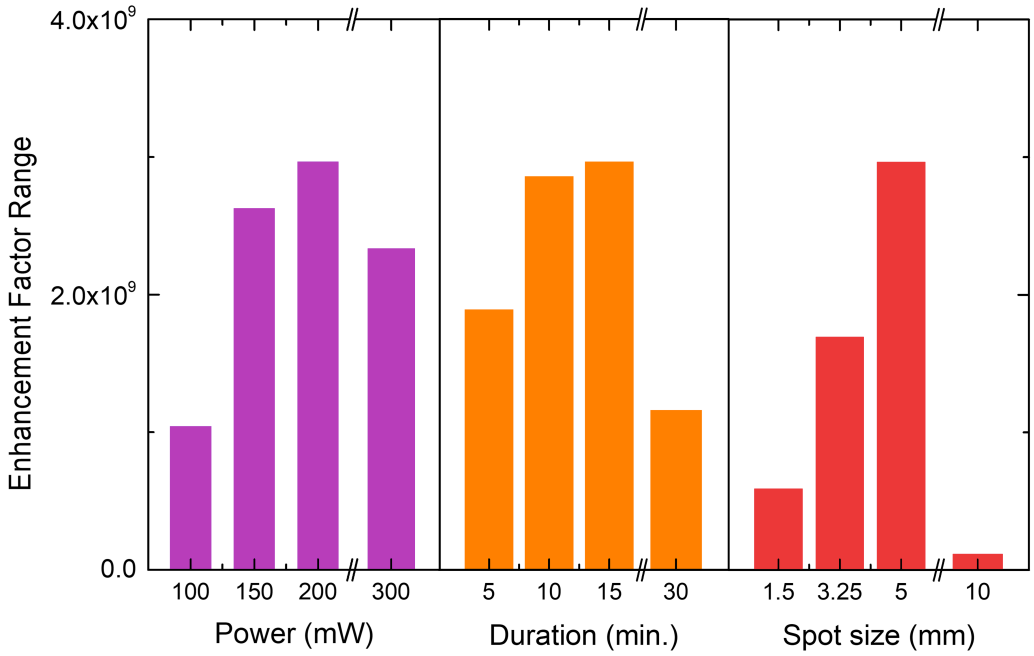

Figure 4.28: Bar graph showing substrate EFs obtained from various photochemical etching parameters applied on silicon keeping the Ag deposition thickness 50 nm and BCB molarity 10^{-5} M. BCB peak at 1653 cm^{-1} is considered in the EF calculation. Power and spot size labels denote the change in the intensity by altering either laser power of the same beam or the modulating the beam spot in the same power level.

EF is calculated not only from the experimental data, it is also derived from the calculated electric field distribution around the structure of which absolute squares denote the field intensity [30]. The product of the enhancement of the incoming field at the excited wavelength and Raman scattered wavelength constitutes the enhancement factor. It is approximated as $EF = \mid E/E_0 \mid^4$ where E is the enhanced electric field distribution around the morphology compared to incoming field E_0. Apart from the EF factor, the plasmon response itself is manifested in the scattering spectra of the structure. Scattering spectra can be obtained both experimentally e.g from the dark-field imaging, and numerically from the FDTD simulations solving for the varying wavelengths. Experimental results of dark-field imaging and spectra are shown in Figure 4.29 and 4.30 b) section. Since a contribution from transmittance cannot be expected in the visible range, the reflectance spectrum can be helpful to speculate about the absorption spectrum of the nanostructures. However, as shown in

the theoretical part, one would expect dominating contribution from scattering. Besides experiments, both FDTD calculated field distribution of a simplified model and scattering response are shown in Figure 4.31 and 4.32. The substrate model is simplified in order to save computational costs and focus on the basic features such as metal thickness dependence and nanoparticle material placed in a sharp nano-hole. A silicon blaze grating structure is coated with Ag and Au with 25 nm and 50 nm thickness. PML boundary conditions are applied and a plane-wave incident from the z-axis downwards polarized in x-axis is sent to the structure. By varying coating thickness, different enhancements of the fields are obtained. For instance, 50 nm Ag has 2.5 times more enhancement than 25 nm Ag, while 50 nm Au has 1.75 times more enhancement than 25 nm Au under the same excitation wavelength with the Raman setup. In the below figure, AgNP exhibits 1.5 times more enhancement than AuNPs in the same nanohole under 532 nm illumination. Though the models are far from the complexity of the real substrate, resulting silicon nanostructures are essentially the composition of the sharp nano-holes depicted in the model varying in size and distribution within a larger structure. Thus, scattering spectra and enhancement levels may not reflect its exact potential and spectral trend, but, there is a correlation within the parameters of thickness, material, and size. The main specific result is that 50 nm Ag coated silicon nanostructures exhibit the best enhancement and plasmon response under both 532 nm and 660 nm illuminations. To be more accurate in terms of the shape of the structures, a model based on SEM image is simulated with the same boundary conditions with 1 nm mesh size as shown in Figure 4.33. The structures enhance incoming field under 532 nm 1.5 times larger than that of 660 nm.

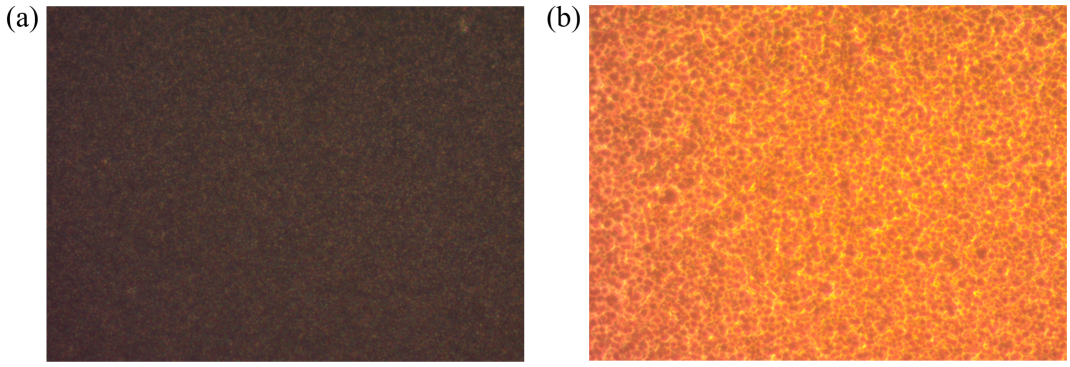

Figure 4.29: Dark field images of a)only roughened silicon and b)50 nm Ag deposited silicon SERS substrate via inverted microscope from 100x objective.

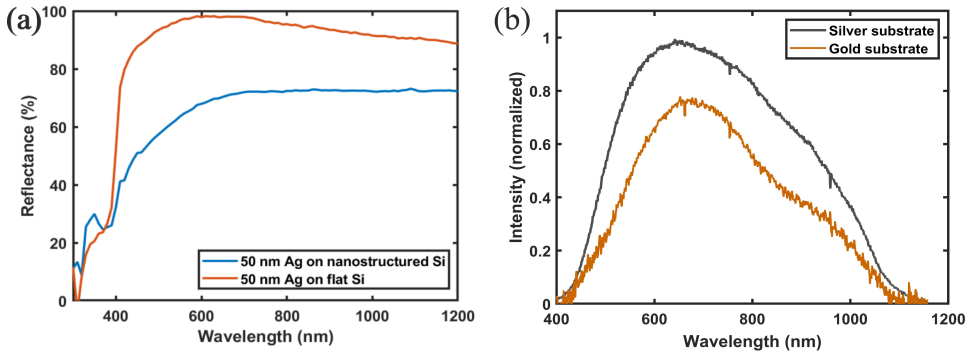

Figure 4.30: a) Reflectance spectra of 50 nm Ag on flat and nanostructured Si. The dip around 400 nm can be attributed to absorption of the substrate. b) Dark-field scattering spectra of 50 nm Ag and Au deposited substrates.

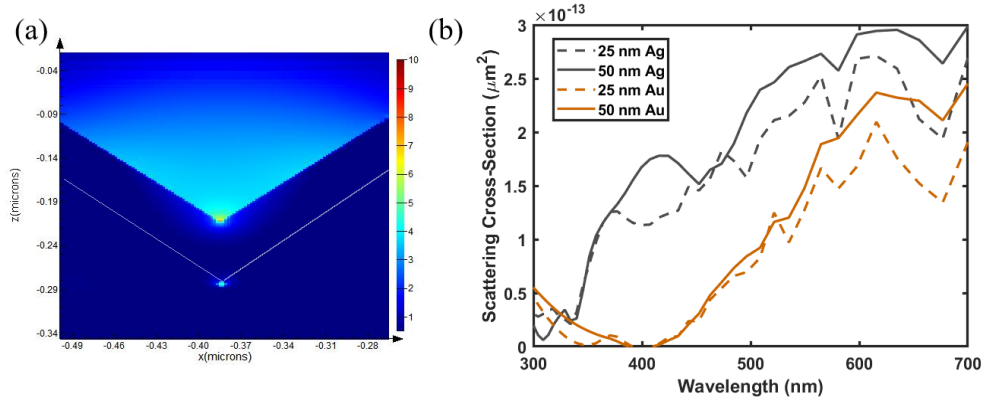

Figure 4.31: a) Simplified FDTD simulation model of the substrate showing the Ag/Au coating on a Si trench. b) Scattering cross-section spectra obtained from a) by changing coating thickness and material on Si.

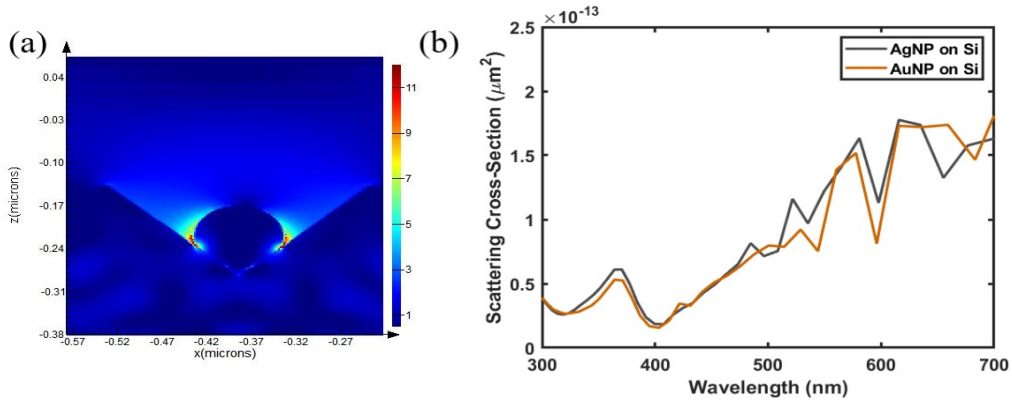

Figure 4.32: a) FDTD simulation of AgNP on a Si trench. b) Simulated scattering cross-section spectra of AgNP and AuNP.

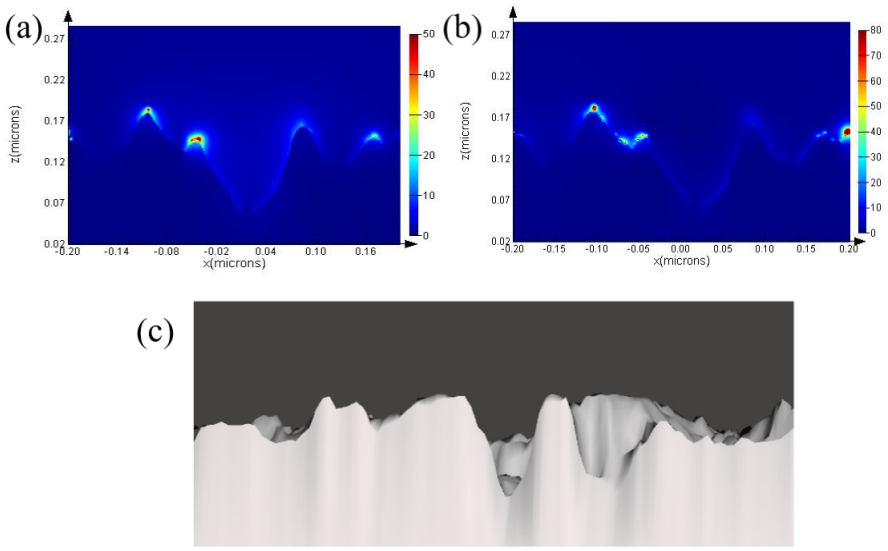

Figure 4.33: FDTD simulations of nanoholes made of Ag excited under a) 660 nm and b) 532 nm based on the model c) which converted from SEM images of Ag coated substrate. Color bars are arbitrary.

4.3.1 Further Discussion

The dipole consideration within the framework of the electrostatic approach given in the theoretical survey is not sufficient for the explanation of these structures' enhancement. Since there is a complex morphology in the resultant nanostructures, plasmonic enhancement must be considered as a mixture of different modes. For instance, silver coated nano-holes have depths in the order of 100 nm, which can be evaluated as Mie scattering [32, 58], and the complex shape and relatively big size imply higher-order modes other than dipole resonance. However, nano-holes have also small (compared to their size and wavelength) ridges within them, along with small resultant nanoparticles, and metal spheres coming from the imperfect nature of the metal evaporation. Those small particles can be considered within the framework of dipole resonance, electrostatic approximation, and Rayleigh scattering. So, the overall enhancement can be viewed as the addition of different modes that are majorly due to complex geometry. And all these effects that are measured via dark field and Raman spectroscopy itself are the projection of near-field effects measured by far-field devices.

CHAPTER 5

CONCLUSION

In the essence of SERS studies, electric-field enhancement within close range of various rough and metal structures lies. Among many fabrication methods, surface nanostructuring techniques fulfill sufficient rough surface configurations. Some of those methods are costly in terms of time and fabrication, while some of them have highly irreproducible albeit being simple. Photo-induced chemical etching is one of the methods that provide adequate roughness due to reaction dynamics, while reactions are controlled via illumination. In this thesis work, the effect of two main fabrication parameters of photochemical nanostructuring of silicon-based SERS substrates on the enhancement is demonstrated. First of all, the enhancement mechanism due to metal structure size and type is shown throughout the paper both numerically and experimentally. Secondly, enhancement is significantly affected by changes in the photochemical etching parameters of silicon. The first parameters alter the plasmon response of the metal material itself with thickness and size control, whereas the second parameters alter the silicon surface due to the etching reaction mechanism initiated by illumination and sustained via etchant and oxidant dynamics. Silicon surface roughness, in this case, nano-hole structure density and size are directly related to the hot-spot density with the addition of metal deposition. By employing a suitable optical setup with a coherent light source and beam shaping components, photochemical etching parameters are optimized. It is achieved by a 532 nm CW laser with adjustable powers and a digital micromirror device as a spatial modulator. As a result; large-area, homogeneously distributed, non-periodic rough silicon surfaces are fabricated in short periods with controllable beam size, power, duration, and periodicities in a broad spectrum of scattering responses.

Nano-fabricated structures are deposited with silver and gold thin film with different thicknesses or decorated with nanoparticles with different growth times to represent the enhancement dependence on the metal structure. An increase of metal component size does not show constant enhancement, instead, enhancement reaches an optimal value with an intermediate metal structure size level comparable with nanohole sizes. The second comparison is made among different textured Si with the same metal thickness. Likewise, intermediate values of etchant/oxidant concentration, laser power, spot size, and duration supplied the optimal enhancement in SERS spectra. It is due to the fact that intermediate values of etching parameters show the most frequent distribution of nano-holes on the Si surface, while a further increase of those parameters limits the etching reaction. By keeping some other parameters constant such as silicon wafer type, crystal orientation, laser wavelength, etc. homogeneous and reproducible SERS substrates are fabricated. To further test the applicability and reproducibility of the structures, spectra of various analyte molecules are measured such as BCB, CV, R6G, and ammonium nitrate. BCB is shown to exhibit its Raman spectrum down to nM orders on the substrates with 50 nm Ag coating and 90% Si nanohole coverage. Furthermore, the use of costly metals such as silver and gold is less than commercial substrates. Considering both thin film and nanoparticle decoration on Si, structured Si areas significantly increase enhancement levels compared to non-illuminated areas. Moreover, changing roughness provides differing templates for nanoparticle growth on the Si surface and increases the hot-spot formations.

Being parallel to the experimental measurements, FDTD simulations also confirm significant near-field enhancements around the structures. Enhancements under 532 nm illumination observed to be larger compared to red spectral region. Ag deposition generally exhibit more enhancement than Au, which also depends on the analyte molecule and excitation wavelength at the same time. As a potential application possibilities, these fabricated structures may have a use in various systems that employ nanoparticles such as sensing other than Raman scattering, photovoltaics, catalysis, etc.

REFERENCES

[1] C. Vannier, B.-S. Yeo, J. Melanson, and R. Zenobi, "Multifunctional microscope for far-field and tip-enhanced raman spectroscopy," *Review of Scientific Instruments*, vol. 77, no. 2, p. 023104, 2006.

[2] X. N. He, Y. Gao, M. Mahjouri-Samani, P. N. Black, J. Allen, M. Mitchell, W. Xiong, Y. S. Zhou, L. Jiang, and Y. F. Lu, "Surface-enhanced raman spectroscopy using gold-coated horizontally aligned carbon nanotubes," *Nanotechnology*, vol. 23, p. 205702, apr 2012.

[3] S. Fateixa, H. I. S. Nogueira, and T. Trindade, "Surface-enhanced raman scattering spectral imaging for the attomolar range detection of crystal violet in contaminated water," *ACS Omega*, vol. 3, no. 4, pp. 4331–4341, 2018. PMID: 31458659.

[4] E. Nalbant Esenturk and A. R. Hight Walker, "Surface-enhanced raman scattering spectroscopy via gold nanostars," *Journal of Raman Spectroscopy*, vol. 40, no. 1, pp. 86–91, 2009.

[5] L.-L. Tay, *Surface Plasmons*, pp. 1186–1195. New York, NY: Springer New York, 2016.

[6] B. G. Rasheed and M. A. Ibrahem, "Laser micro/nano machining of silicon," *Micron*, vol. 140, p. 102958, 2021.

[7] D. Dudley, W. M. Duncan, and J. Slaughter, "Emerging digital micromirror device (dmd) applications," *MOEMS Display and Imaging Systems*, vol. 4985, p. 14, 2003.

[8] E. Smith and G. Dent, "Modern raman spectroscopy: A practical approach," 2005.

[9] R. Pilot, R. Signorini, C. Durante, L. Orian, M. Bhamidipati, and L. Fabris, "A review on surface-enhanced raman scattering," *Biosensors*, vol. 9, no. 2, 2019.

[10] L. Ouyang, W. Ren, L. Zhu, and J. Irudayaraj, "Prosperity to challenges: recent approaches in sers substrate fabrication," *Reviews in Analytical Chemistry*, vol. 36, no. 1, p. 20160027, 2017.

[11] G. Gervinskas, G. Seniutinas, J. S. Hartley, S. Kandasamy, P. R. Stoddart, N. F. Fahim, and S. Juodkazis, "Surface-enhanced raman scattering sensing on black silicon," *Annalen der Physik*, vol. 525, pp. 907–914, 2013.

[12] Z. Cui, L. Lu, Y. Guan, S. Ramakrishna, and M. Hong, "Enhancing sers detection on a biocompatible metallic substrate for diabetes diagnosing," *Opt. Lett.*, vol. 46, pp. 3801–3804, Aug 2021.

[13] S. Bai, Y. Du, C. Wang, J. Wu, and K. Sugioka, "Reusable surface-enhanced raman spectroscopy substrates made of silicon nanowire array coated with silver nanoparticles fabricated by metal-assisted chemical etching and photonic reduction," *Nanomaterials*, vol. 9, 2019.

[14] K. W. Kolasinski, D. Mills, and M. Nahidi, "Laser assisted and wet chemical etching of silicon nanostructures," *Journal of Vacuum Science Technology A: Vacuum, Surfaces, and Films*, vol. 24, pp. 1474–1479, 2006.

[15] C. Zhang, S. Z. Jiang, Y. Y. Huo, A. H. Liu, S. C. Xu, X. Y. Liu, Z. C. Sun, Y. Y. Xu, Z. Li, and B. Y. Man, "Sers detection of r6g based on a novel graphene oxide/silver nanoparticles/silicon pyramid arrays structure," *Optics Express*, vol. 23, p. 24811, 2015.

[16] T. T. K. Chi, N. T. Le, B. T. T. Hien, D. Q. Trung, and N. Q. Liem, "Preparation of sers substrates for the detection of organic molecules at low concentration," *Communications in Physics*, vol. 26, p. 261, Jan. 2017.

[17] S. Enoch and N. Bonod, *Plasmonics*. 2012.

[18] M. Fleischmann, P. Hendra, and A. McQuillan, "Raman spectra of pyridine adsorbed at a silver electrode," *Chemical Physics Letters*, vol. 26, no. 2, pp. 163–166, 1974.

[19] M. Moskovits, "Surface roughness and the enhanced intensity of raman scattering by molecules adsorbed on metals," *The Journal of Chemical Physics*, vol. 69, no. 9, pp. 4159–4161, 1978.

[20] S. Schlücker, "Nanoscale chemical mapping using three-dimensional adiabatic compression of surface plasmon polaritons," *Angewandte Chemie International Edition*, vol. 53, no. 19, pp. 4756–4795, 2014.

[21] S.-Y. Ding, J. Yi, J.-F. Li, B. Ren, D.-Y. Wu, R. Panneerselvam, and Z.-Q. Tian, "Nanostructure-based plasmon-enhanced raman spectroscopy for surface analysis of materials," *Nature Reviews Materials*, vol. 1, p. 16021, Apr 2016.

[22] E. C. Le Ru and P. G. Etchegoin, "Chapter 1 - a quick overview of surface-enhanced raman spectroscopy," in *Principles of Surface-Enhanced Raman Spectroscopy* (E. C. Le Ru and P. G. Etchegoin, eds.), pp. 1–27, Amsterdam: Elsevier, 2009.

[23] R. J. Clarke and A. Oprysa, "Fluorescence and light scattering," *Journal of Chemical Education*, vol. 81, no. 5, p. 705, 2004.

[24] C. V. Raman, "A new radiation," *Indian Journal of physics*, vol. 2, pp. 387–398, 1928.

[25] M. D. Fontana and P. Bourson, "Microstructure and defects probed by raman spectroscopy in lithium niobate crystals and devices," *Applied Physics Reviews*, vol. 2, no. 4, p. 040602, 2015.

[26] E. Fort, "Plasmonics," *Optics in Instruments*, pp. 179–216, 2013.

[27] E. C. Le Ru and P. G. Etchegoin, "Chapter 3 - introduction to plasmons and plasmonics," in *Principles of Surface-Enhanced Raman Spectroscopy* (E. C. Le Ru and P. G. Etchegoin, eds.), pp. 121–183, Amsterdam: Elsevier, 2009.

[28] R. H. RITCHIE, "Plasma Losses by Fast Electrons in Thin Films," *Physical Review*, vol. 106 N.5, no. 5, p. 8, 1956.

[29] K. A. Willets and R. P. V. Duyne, "Localized surface plasmon resonance spectroscopy and sensing," *Annual Review of Physical Chemistry*, vol. 58, pp. 267–297, 2007.

[30] L. Novotny and B. Hecht, *Principles of Nano-Optics*. Cambridge University Press, 2 ed., 2012.

[31] W. L. Barnes, "Particle plasmons: Why shape matters," *American Journal of Physics*, vol. 84, pp. 593–601, 8 2016.

[32] G. Mie, "Beiträge zur optik trüber medien, speziell kolloidaler metallösungen," *Annalen der Physik*, vol. 330, no. 3, pp. 377–445, 1908.

[33] M. I. Tribelsky and B. S. Luk'yanchuk, "Anomalous light scattering by small particles," *Physical Review Letters*, vol. 97, 2006.

[34] E. Prodan, C. Radloff, N. J. Halas, and P. Nordlander, "A hybridization model for the plasmon response of complex nanostructures," *Science*, vol. 302, no. 5644, pp. 419–422, 2003.

[35] D. M. Sullivan, *Three-Dimensional Simulation*, pp. 79–108. 2000.

[36] W. Lang, "Silicon microstructuring technology," *Materials Science and Engineering: R: Reports*, vol. 17, no. 1, pp. 1–55, 1996.

[37] A. A. Ensafi, F. Rezaloo, and B. Rezaei, "Electrochemical sensor based on porous silicon/silver nanocomposite for the determination of hydrogen peroxide," *Sensors and Actuators B: Chemical*, vol. 231, pp. 239–244, 2016.

[38] J. Bonse, S. V. Kirner, S. Höhm, N. Epperlein, D. Spaltmann, A. Rosenfeld, and J. Krüger, "Applications of laser-induced periodic surface structures (LIPSS)," in *Laser-based Micro- and Nanoprocessing XI* (U. Klotzbach, K. Washio, and R. Kling, eds.), vol. 10092, pp. 114 – 122, International Society for Optics and Photonics, SPIE, 2017.

[39] B. K. Nayak, M. C. Gupta, and K. W. Kolasinski, "Ultrafast-laser-assisted chemical restructuring of silicon and germanium surfaces," *Applied Surface Science*, vol. 253, no. 15, pp. 6580–6583, 2007. Proceedings of the Fifth International Conference on Photo-Excited Processes and Applications.

[40] I. Talian, K. B. Mogensen, A. Oriňák, D. Kaniansky, and J. Hübner, "Surface-enhanced raman spectroscopy on novel black silicon-based nanostructured surfaces," *Journal of Raman Spectroscopy*, vol. 40, no. 8, pp. 982–986, 2009.

[41] L. Koker and K. W. Kolasinski, "Photoelectrochemical etching of si and porous

si in aqueous hf," *Physical Chemistry Chemical Physics*, vol. 2, pp. 277–281, 2000.

[42] L. Koker and K. W. Kolasinski, "Laser-assisted formation of porous si in diverse fluoride solutions: Reaction kinetics and mechanistic implications," *Journal of Physical Chemistry B*, vol. 105, pp. 3864–3871, 2001.

[43] H. S. Mavi, B. G. Rasheed, A. K. Shukla, S. C. Abbi, and K. P. Jain, "Spectroscopic investigations of porous silicon prepared by laser-induced etching of silicon," *Journal of Physics D: Applied Physics*, vol. 34, pp. 292–298, jan 2001.

[44] S. K. Saxena, V. Kumar, H. M. Rai, G. Sahu, R. Late, K. Saxena, A. K. Shukla, P. R. Sagdeo, and R. Kumar, "Study of porous silicon prepared using metal-induced etching (mie): a comparison with laser-induced etching (lie)," *Silicon*, vol. 9, pp. 483–488, 2017.

[45] K. Tsujino and M. Matsumura, "Morphology of nanoholes formed in silicon by wet etching in solutions containing hf and h2o2 at different concentrations using silver nanoparticles as catalysts," *Electrochimica Acta*, vol. 53, no. 1, pp. 28–34, 2007. ELECTROCHEMICAL PROCESSING OF TAILORED MATERIALS Selection of papers from the 4th International Symposium (EPTM 2005) 3-5 October 2005, Kyoto, Japan.

[46] D. Bäuerle, *Etching of Semiconductors*, pp. 339–366. Berlin, Heidelberg: Springer Berlin Heidelberg, 2011.

[47] M. Chelvayohan and C. H. B. Mee, "Work function measurements on (110), (100) and (111) surfaces of silver," *Journal of Physics C: Solid State Physics*, vol. 15, pp. 2305–2312, apr 1982.

[48] X. M. Yang, Z. W. Zhong, E. M. Diallo, Z. H. Wang, and W. S. Yue, "Silicon wafer wettability and aging behaviors: Impact on gold thin-film morphology," *Materials Science in Semiconductor Processing*, vol. 26, pp. 25–32, 2014.

[49] R. Kumar, H. Mavi, and A. Shukla, "Macro and microsurface morphology reconstructions during laser-induced etching of silicon," *Micron*, vol. 39, no. 3, pp. 287–293, 2008.

[50] P. A. Savale, "Physical vapor deposition (pvd) methods for synthesis of thin films: A comparative study," 2016.

[51] *Handbook of Biological Dyes and Stains*, pp. 405–424. John Wiley Sons, Ltd, 2010.

[52] *Handbook of Biological Dyes and Stains*, pp. 71–122. John Wiley Sons, Ltd, 2010.

[53] *Handbook of Biological Dyes and Stains*, pp. 37–69. John Wiley Sons, Ltd, 2010.

[54] E. C. L. Ru, E. Blackie, M. Meyer, and P. G. Etchegoin, "Surface enhanced raman scattering enhancement factors: A comprehensive study," *Journal of Physical Chemistry C*, vol. 111, pp. 13794–13803, 9 2007.

[55] E. C. Le Ru and P. G. Etchegoin, "Chapter 4 - sers enhancement factors and related topics," in *Principles of Surface-Enhanced Raman Spectroscopy* (E. C. Le Ru and P. G. Etchegoin, eds.), pp. 185–264, Amsterdam: Elsevier, 2009.

[56] J. Langer, D. Jimenez de Aberasturi, J. Aizpurua, R. A. Alvarez-Puebla, B. Auguié, J. J. Baumberg, G. C. Bazan, S. E. J. Bell, A. Boisen, A. G. Brolo, J. Choo, D. Cialla-May, V. Deckert, L. Fabris, K. Faulds, F. J. García de Abajo, R. Goodacre, D. Graham, A. J. Haes, C. L. Haynes, C. Huck, T. Itoh, M. Käll, J. Kneipp, N. A. Kotov, H. Kuang, E. C. Le Ru, H. K. Lee, J.-F. Li, X. Y. Ling, S. A. Maier, T. Mayerhöfer, M. Moskovits, K. Murakoshi, J.-M. Nam, S. Nie, Y. Ozaki, I. Pastoriza-Santos, J. Perez-Juste, J. Popp, A. Pucci, S. Reich, B. Ren, G. C. Schatz, T. Shegai, S. Schlücker, L.-L. Tay, K. G. Thomas, Z.-Q. Tian, R. P. Van Duyne, T. Vo-Dinh, Y. Wang, K. A. Willets, C. Xu, H. Xu, Y. Xu, Y. S. Yamamoto, B. Zhao, and L. M. Liz-Marzán, "Present and future of surface-enhanced raman scattering," *ACS Nano*, vol. 14, no. 1, pp. 28–117, 2020.

[57] *Eurachem Guide: The Fitness for Purpose of Analytical Methods – A Laboratory Guide to Method Validation and Related Topics*. 2 ed., 2014.

[58] E. C. Le Ru and P. G. Etchegoin, "Chapter 6 - em enhancements and plasmon resonances: examples and discussion," in *Principles of Surface-Enhanced Ra-*

man Spectroscopy (E. C. Le Ru and P. G. Etchegoin, eds.), pp. 299–365, Amsterdam: Elsevier, 2009.